



Title	Amplification Properties of MgO-Based Magnetic Tunneling Junctions
Author(s)	Konishi, Katsunori
Citation	大阪大学, 2013, 博士論文
Version Type	VoR
URL	https://hdl.handle.net/11094/27504
rights	
Note	

The University of Osaka Institutional Knowledge Archive : OUKA

<https://ir.library.osaka-u.ac.jp/>

The University of Osaka

Amplification Properties of MgO-Based
Magnetic Tunneling Junctions

BY

KATSUNORI KONISHI

MARCH 2013

Amplification Properties of MgO-Based Magnetic Tunneling Junctions

A dissertation submitted to

**THE GRADUATE SCHOOL OF ENGINEERING
SCIENCE**

OSAKA UNIVERSITY

in partial fulfillment of the requirements for the degree of
DOCTOR OF PHILOSOPHY IN ENGINEERING

BY

KATSUNORI KONISHI

MARCH 2013

ABSTRACT

The discovery of giant tunneling magnetoresistance (TMR) in MgO-based magnetic tunnel junctions (MTJs) has accelerated the development of new types of devices. These range from passive devices, such as reading heads in hard disk drives and magnetic random access memory, to active devices, such as microwave oscillators and microwave detectors. In addition to these devices, new types of three terminal devices, so-called spin transistors, have been researched intensively to realize non-volatile logic circuits, as they can perform both logical operations and store information. Many types of spin transistor have been researched theoretically and experimentally, but the power amplification property, which is necessary for logical operations, has not yet been realized in spin transistors at room temperature. In this study, a spin transistor with a novel structure and operating principle is proposed and the amplification properties are evaluated.

The basic structure of the proposed spin transistor consists of an MTJ with a low resistance area product and an electrically isolated metallic wire. Application of current to the metallic wire generates a magnetic field around the wire, inducing magnetization switching of the free layer in the MTJ. Due to the TMR effect, the output power from the MTJ changes as a result of the magnetization switching. If the change in the output power between the parallel and anti-parallel configurations in the MTJ is larger than the input power consumed by the pulse application to the wire, this device can drive the basic cascaded structure and can function as a logic circuit.

By employing micro-fabrication on MgO-based MTJs, which were fabricated by magnetron sputtering, the above structure was produced. Then, its amplification properties were evaluated at room temperature. A power gain of 5.6 was successfully obtained under a bias voltage of 0.4 V. The device scaling was also compared to theoretical calculations and other experimental results.

Next, to further enhance the amplification, amplification properties were evaluated under an effective coercive field, which was reduced by the application of an assisting AC magnetic field. A power gain of 130 and fan-out value (the number of MTJs driven by the output from a single MTJ) of 5.7 were obtained. The non-volatility was also evaluated, and was shown to be sufficient even under an

assisting AC magnetic field. Therefore, this device can be used as a basic component in non-volatile logic devices.

Generally, the frequencies of ferromagnetic resonance are in the gigahertz (GHz) range. Utilizing this characteristic, the radio frequency (RF) amplification properties of the device were evaluated. The static external magnetic field and angular dependency of the voltage gain were systematically investigated and reproduced quantitatively by a simple macro-spin model simulation. Although RF gain does not reach unity, the design principles for the enhancement of the gain factor are discussed.

論文内容の要旨

MgO トンネル障壁を用いた強磁性トンネル接合 (MTJ) 素子において巨大な磁気抵抗効果が発見されたのをきっかけに、MTJ 素子を用いた新たなデバイスの研究が盛んに行われている。その範囲は、ハードディスクドライブにおける読み取りヘッドや固体磁気メモリのように受動素子のもものばかりではなく、マイクロ波発振器やマイクロ波検波器などの能動素子にも及んでいる。これらのデバイスに加え、不揮発性論理回路実現の為に、論理演算機能とスピンの持つ記憶機能を併せ持ったスピントランジスタと呼ばれる三端子デバイスに期待が寄せられている。これまでに様々なスピントランジスタに関する実験が行われてきたが、室温において論理演算に必要な不可欠な増幅作用は実現されていなかった。そこで本研究においては、新たな構造・原理を持ったスピントランジスタを提案・作製し、増幅特性を中心に評価をおこなった。

提案する新たなスピントランジスタは低面積抵抗の MTJ 素子とそれとは電氣的に絶縁された金属線から構成されており、金属線に電流を流すことで、金属線周りに磁界が発生し、MTJ 素子のフリー層の磁化反転を誘起する。これにより MTJ 素子の出力が変化し、金属線に入力した電力よりも、磁化反転による出力の変化分が大きければ、このデバイスは増幅作用を持ったデバイスであるといえる。

マグネトロンスパッタリングにより作製された MgO 障壁を有する MTJ 素子に微細加工を施し、上記構造を作製し、室温における増幅作用の評価を行ったところ、0.4 V のバイアス電圧下において電力増幅率 5.6 を得ることに成功した。さらに、実験で得られた値と理論値を比較することで、デバイスの設計方針を示した。

次に増幅率のさらなる増大のために、外部からアシスト交流磁界を印加し有効的な保磁力を下げた状態での評価を行った。その結果、電力増幅率 130 及び 5.7 のファンアウト（一つの MTJ 素子の出力により駆動させることが可能な MTJ 素子の数であり、このデバイスにおける重要なパラメータの一つ）を得た。同時に不揮発性についても言及し、同スピントランジスタがアシスト交流磁界下でも十分な不揮発機能を有しており、不揮発性論理回路の基本素子として使える可能性を示した。

一般的な強磁性体の共鳴周波数は GHz 帯にある。この性質を利用して、上記スピントランジスタにおける高周波の増幅作用についても評価を行った。外部磁場の強度と角度を変えながら増幅率を系統的に測定した結果はマクロスピンシミュレーションと定性的に一致した。得られた増幅率は 1 未満ではあったものの、1 を超える増幅率を得る為の MTJ 素子の設計方針を示した。

Contents

Contents	6
Chapter 1 Introduction.....	7
1.1 Magnetoresistance (MR) Effect	7
1.2 Tunneling Magnetoresistance (TMR) Effect.....	8
1.3 Spin-Transfer Effect.....	13
1.3 Spin Dynamics	16
1.5 Objectives of this Study	28
Chapter 2 Device scaling (theoretical derivation).....	30
2.1 Concept of the current-field driven spin transistors	30
2.2 Scaling of current-field driven spin transistors	32
2.3 Concept of the spin torque driven spin transistor.....	41
2.4 Scaling of spin torque driven spin transistor	42
2.5 Comparison of characteristics of spin transistors	44
Chapter 3 Experimental method	47
3.1 Film fabrication.....	47
3.2 Micro-fabrication.....	48
3.3 Measurements.....	51
Chapter 4 Results and Discussion	54
4.1 Power amplification	54
4.2 Realization of Fan-out.....	60
4.3 RF amplification.....	68
Chapter 5 Conclusion	75
Acknowledgement.....	80
References	82
List of Publications	87
List of Conference Presentations	89
List of Grant.....	93

Chapter 1 Introduction

In this chapter, the magnetoresistance (MR) effect, is the most important effect in spintronics, and magnetoresistive devices are introduced. Then, the basic theory is described, and finally, the objectives of this thesis are outlined.

1.1 Magnetoresistance (MR) Effect

The history of spintronics is closely related to the development of the magnetoresistance (MR) effect^{[1],[2]}. Generally, phenomena in which the resistance changes when a magnetic field is applied are referred to as MR effects. Widespread interest in MR effects began with the anisotropic magnetoresistance (AMR) effect^[3]. The AMR effect is a phenomenon in which the electrical resistance depends on the relative angle between the directions of magnetization and current flow. The origin of this effect is the spin-orbit interaction, and it is larger in materials with large orbital magnetic moments. The AMR effect was utilized in the reading head of hard disk drives (HDDs), which is described in the section on spin devices (Section 1.4).

Further interest in magnetic layers began in 1986 with the discovery of interlayer exchange coupling, which is the interaction between the magnetizations of two ferromagnetic layers separated by an ultrathin, non-ferromagnetic layer. In particular, the discovery of anti-ferromagnetic coupling in the Fe/Cr/Fe system by Grünberg *et al.*^[4] aroused great interest and it led to the discovery of the Giant Magneto Resistane (GMR) effect independently in the groups of Grünberg^[4] and Fert^[5], for which they won the Nobel Prize in Physics in 2008. GMR is the change in resistance that occurs when the magnetizations of two ferromagnetic layers change. Fig. 1 shows an example of the GMR effect in Fe/Cr/Fe anti-ferromagnetically coupled multilayers, as reported by Fert's group. When the magnetizations of two Fe layers separated by a Cr layer are in an anti-parallel state to one another with no external magnetic field, as they are when anti-ferromagnetically coupled, the sample has a relatively large resistance. The magnetizations of the Fe layers can be brought into a parallel state by applying an external magnetic field. In the parallel state, the resistance of the system is reduced. The total change in resistance is typically up to a few tens of percent. Most of the early works on GMR focused on sample geometries in which a current flows in the film plane (CIP). In another geometry type, the current flows perpendicular to the film plane (CPP).

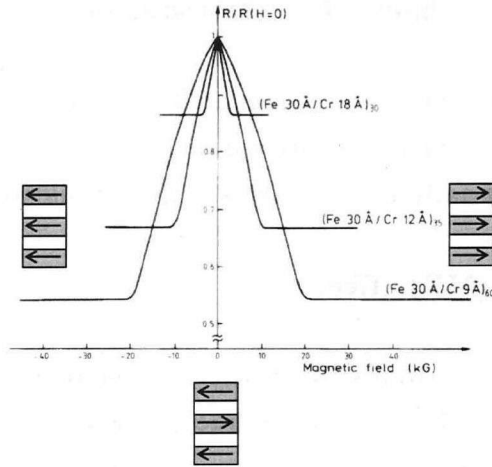


Fig. 1 An example of the GMR effect in Fe/Cr/Fe anti-ferromagnetically coupled multilayers, as reported by Fert *et al.*^[5] When the external magnetic field is zero, the magnetizations of the Fe layers separated by the Cr spacer layer are in the anti-parallel state, resulting in a relatively large resistance. However, under a large external magnetic field, the magnetizations of Fe layers are in the parallel state and the resistance is reduced.

The MR ratio (MR) is defined by following equation,

$$MR = \frac{R_{AP} - R_P}{R_P} \times 100[\%] \quad \dots (1.1)$$

where R_P , and R_{AP} are the resistance in the parallel and anti-parallel states, respectively.

1.2 Tunneling Magnetoresistance (TMR) Effect

A GMR device consists of a nonmagnetic layer sandwiched by ferromagnetic layers. Here, the tunneling magnetoresistance (TMR) effect is discussed. The typical structure of a TMR device is a tri-layer comprising ferromagnetic/insulator/ferromagnetic layers. A thin insulator layer (e.g., Al-Ox, MgO) is used as a spacer layer instead of the nonmagnetic metal used in GMR devices. This junction is called a magnetic tunnel junction (MTJ). Compared with the GMR device, the MTJ has a relatively large Resistance Area (RA) product, because the tunnel barrier is an insulator. The RA has an exponential dependency on the insulator layer thickness. In the MTJ, the spin-dependent electron-flow direction is usually perpendicular to the

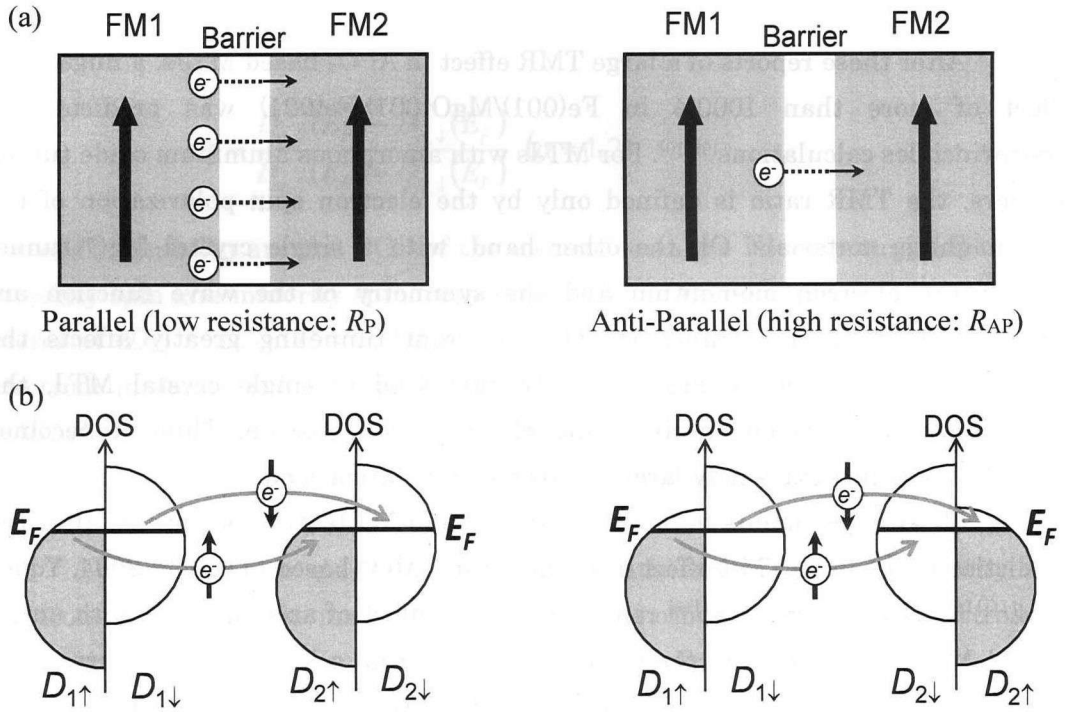


Fig. 2 (a) Schematic illustrations of the TMR effect in MTJs. The parallel magnetization configuration (left figure) exhibits low resistance and the antiparallel magnetization configuration (right figure) high resistance. (b) Schematic illustrations of the TMR effect with the spin-dependent band structures following Julliere's model. $D_{1\uparrow}$ and $D_{1\downarrow}$ respectively denote the density of states at the Fermi surface (E_F) for the majority-spin and minority-spin bands in FM1, and $D_{2\uparrow}$ and $D_{2\downarrow}$ respectively denote the density of states at E_F for the majority-spin and minority-spin bands in FM2.

plane of the film, i.e., in the CPP configuration. A schematic image of the TMR effect is shown in Fig. 2(a). The first report of the TMR effect was made by Julliere^[6] in 1975,

using Fe/Ge/Co MTJs. A TMR ratio of around 10% was obtained only under low temperature conditions. The TMR ratio at room temperature, however, was too small and did not attract much interest for device applications. In 1995, a significant discovery in relation to the TMR effect was made by Miyazaki *et al.*^[7] and Moodera *et al.*^[8] They observed a large TMR ratio (~20%) at room temperature for MTJs with an amorphous aluminum oxide (Al-O_x) insulating barrier. The obtained MR ratio was larger than that expected from GMR devices at that time. Al-O_x based MTJs were also used as reading heads in HDDs.

After these reports of a large TMR effect in Al-O_x-based MTJs, a huge TMR effect of more than 1000% in Fe(001)/MgO(001)/Fe(001) was predicted by first-principles calculations^{[9],[10]}. For MTJs with amorphous aluminum oxide tunnel barriers, the TMR ratio is defined only by the electron spin polarization of the ferromagnetic materials. On the other hand, with a single crystal MgO tunnel barrier, the electron momentum and the symmetry of the wave function are conserved in tunneling transport. This coherent tunneling greatly affects the conductance in the band gap states. In this kind of single crystal MTJ, the conductance depends on specific band electron transmission. Thus, it becomes possible to conduct extremely large electron spin polarizations.

Many experiments to fabricate MgO-based MTJs were performed after the prediction of the huge TMR effect in single crystal MgO based MTJs. In 2004, Yuasa *et al.*^{[11],[12]} and Parkin *et al.*^[13] reported a TMR effect of around 200% with single crystal MgO-MTJs at room temperature. Afterwards, a TMR effect greater than 200% was observed in a CoFeB/MgO/CoFeB MTJ^[14], which was fabricated by sputtering. Although CoFeB layers are amorphous in an as-grown state, they have a crystalline bcc (001) structure after post-annealing. These CoFeB/MgO/CoFeB MTJs are more suitable for mass production than those produced with molecular beam epitaxy (MBE), and this has enabled significant progress to be made in research and development (they are used also in this study). Until now, TMR ratios of around 600% at room temperature and 1000% at low temperature^[15] have been obtained using CoFeB electrodes and an MgO barrier. Besides the high TMR ratio, the RA can be reduced in MgO-based MTJs. This is another good property of the MgO barrier, since low resistance is required in the actual device. Utilizing the high MR ratio and low RA in MgO-based MTJs, research and development of spin devices,

such as a HDD and magnetoresistive random access memory (MRAM), have accelerated.

To understand the TMR effect, Julliere's theoretical model (schematically shown in Fig. 2 (b)) is simple and powerful. In this model, the tunnel probability is assumed to be the same for all Bloch states in the electrodes, and the spin polarization of the tunneling electrons (P_1 for FM1 and P_2 for FM2) is expressed as a function of the spin-dependent density of states (DOS) of the ferromagnetic electrode material,

$$\text{MR} = \frac{2P_1P_2}{1 - P_1P_2} \times 100[\%] \quad \dots (1.2)$$

where

$$P_\alpha = \frac{D_{\alpha,\uparrow}(E_F) - D_{\alpha,\downarrow}(E_F)}{D_{\alpha,\uparrow}(E_F) + D_{\alpha,\downarrow}(E_F)} \quad (\alpha = 1, 2) \quad \dots (1.3)$$

Here, $D_{\alpha,\uparrow}$ and $D_{\alpha,\downarrow}$ are the DOS of the electrodes at the Fermi energy (E_F) for the majority spin and minority spin, respectively. When the electrode is a nonmagnetic material ($D_{\alpha,\uparrow} = D_{\alpha,\downarrow}$), $P = 0$, following eq. (1.3). However, when the DOS of the electrode materials is fully spin polarized ($[D_{\alpha,\uparrow} = 1$ and $D_{\alpha,\downarrow} = 0]$ or $[D_{\alpha,\uparrow} = 0$ and $D_{\alpha,\downarrow} = 1]$), $P = 1$. In MgO-based MTJs, the DOS of the Δ_1 band, in which electrons mainly contribute to conduction, is fully spin polarized, leading to a huge TMR effect.

When the two magnetization configurations are parallel, majority spin electrons tunnel into the majority spin band of the other ferromagnetic electrode; in this situation, the conductance is expressed as σ^{++} . For the minority spin carriers, the electrons tunnel from one minority spin band into the other minority spin band (σ^{--}). Conversely, in the antiparallel configuration, the majority spin electrons tunnel into the minority spin band of the other ferromagnetic electrode (σ^{+-}), and from the minority spin band into the majority spin band (σ^{-+}). The total electron current (J) under the P and AP states can be written as follows using the sum of the conductances (σ^{++} , σ^{+-} , σ^{-+} , σ^{--}),

$$\begin{aligned} J_P &= J_\uparrow + J_\downarrow = (\sigma^{++} + \sigma^{--})V \quad (\text{in P-states}) \\ J_{AP} &= J_\uparrow + J_\downarrow = (\sigma^{+-} + \sigma^{-+})V \quad (\text{in AP-states}) \end{aligned} \quad \dots (1.4).$$

The above discussion considers only collinear spins. Hereafter, the tunnel conductance for non-collinear spins is discussed (i.e., the magnetization

configurations are not parallel or anti-parallel but intermediate states). Here, the angle between the directions of the magnetization in the pinned and free layers is θ , as shown in Fig. 3. The projection between the majority spin of FM1 to the majority spin of FM2 is $\cos(\theta/2)$. Here, the factor of 1/2 is due to the spin. For the minority-to-minority spin, the projection is also $\cos(\theta/2)$. For the majority-to-minority (or minority-to-majority) spin, it is $\cos[(\pi-\theta)/2] = \sin(\theta/2)$. The probabilities of these spin states are given by the squares of the projections. Thus, the current for the MTJ can be written as eq. (1.5).

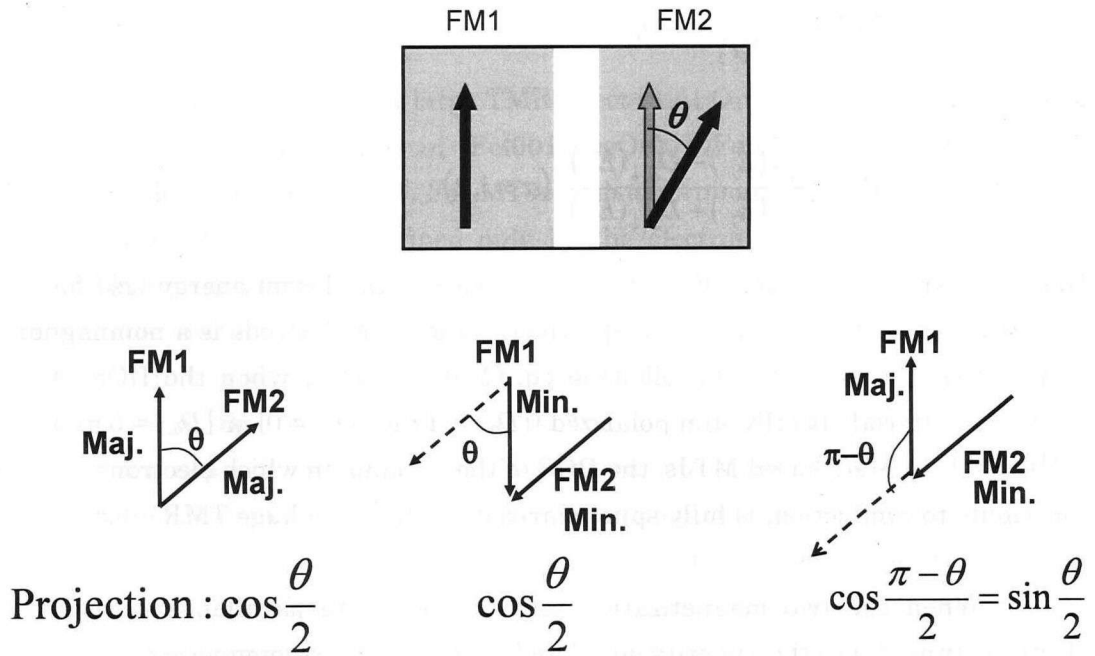


Fig. 3 Schematic illustration of tunnel conductance for the non-collinear magnetization configuration. The angle between the magnetization directions of FM1 and FM2 is θ . The figures at the bottom show projections of the majority-to-majority, minority-to-minority, and majority-to-minority (minority-to-majority) spins.

$$\begin{aligned}
J &= J_{\uparrow} + J_{\downarrow} \\
&= \left[(\sigma^{++} + \sigma^{--}) \cos^2(\theta/2) + (\sigma^{+-} + \sigma^{-+}) \sin^2(\theta/2) \right] V \\
&= \left[(\sigma^{++} + \sigma^{--}) \frac{1 + \cos\theta}{2} + (\sigma^{+-} + \sigma^{-+}) \frac{1 - \cos\theta}{2} \right] V \quad \dots (1.5). \\
&= \left(\frac{\sigma^{++} + \sigma^{--} + \sigma^{+-} + \sigma^{-+}}{2} + \frac{\sigma^{++} + \sigma^{--} - \sigma^{+-} - \sigma^{-+}}{2} \cos\theta \right) V
\end{aligned}$$

From eq. (1.5), the conductance of the system σ can be written as follows,

$$\begin{aligned}
\sigma &= \frac{\sigma^{++} + \sigma^{--} + \sigma^{+-} + \sigma^{-+}}{2} + \frac{\sigma^{++} + \sigma^{--} - \sigma^{+-} - \sigma^{-+}}{2} \cos\theta \quad \dots (1.6). \\
&= \sigma_0 + \Delta\sigma \cos\theta
\end{aligned}$$

Here, σ_0 is average conductance between the parallel and anti-parallel magnetization configurations and $\Delta\sigma$ is the change in the conductance from the parallel to the anti-parallel state. The conductance of the MTJ depends on the relative angle θ , as shown in equation (1.6).

1.3 Spin-Transfer Effect

The spin-transfer effect^{[16],[17]}, which has gained much attention in spintronics, is described in this section. Since the spin-torque effect becomes important when the device size becomes smaller, the ultra-low consumption device is expected to utilize spin-transfer torque. Many phenomena have been discovered using the spin-transfer effect, such as spin-injection magnetization switching, the spin-torque oscillator, and the spin-torque diode effect.

The spin-transfer effect occurs by the exchange interaction between electron spin and localized spin. To discuss the spin-transfer effect simply, the model of a magnetic nano-pillar is employed, which is schematically shown in Fig. 4. The device consists of ferromagnetic layer 1 (FM1) / non-magnetic layer 1 (NM1) / ferromagnetic layer 2 (FM2) / non-magnetic layer 2 (NM2). FM1 is called the pinned layer (or fixed layer) and FM2 the free layer. When an electron goes from FM1 to FM2 via NM1, the spins of the conduction electrons become polarized by the interaction between the localized spins in FM1. The polarized electrons are injected into FM2 through NM1 (here, the length of NM2 is so small that spins can conserve

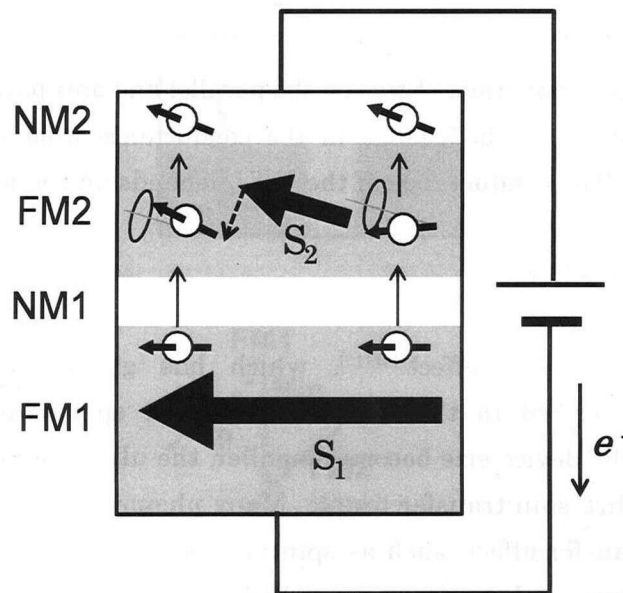


Fig. 4 Schematic illustration of spin-transfer torque (shown as the dotted arrow) in a magnetic nano-pillar. Electrons are polarized by passing through the ferromagnetic layer (FM1) and go into the ferromagnetic layer (FM2). The spin interacts with the local spin in FM2 S_2 , leading to spin torque. In this current direction, the directions of S_1 and S_2 become parallel.

their direction). The injected spins interact again with the localized spins in FM2 and the direction of the spins change to that of the spin in FM2. At this time, the spins of electrons receive angular momentum from localized spins in FM2. The total angular momentum must be conserved in the system (angular momentum conservation law), and hence, localized spins also receive angular momentum from electron spins (FM1 also receives angular momentum when the conduction electron is polarized; however, the influence of this can be ignored because FM1 is completely fixed). The applied angular momentum from electrons to FM2 acts as

torque, and therefore, this is referred to as spin-transfer torque (or simply spin torque). When the effect of spin torque is sufficiently large, the local spin in FM2 can be switched.

Next, the mathematical expression for spin-transfer torque is derived. The localized spin in FM1 and FM2 are written as \vec{S}_1 and \vec{S}_2 , respectively. From the low angular conservation, the spin torque can be defined as the difference between the spin current \vec{J}_{s1} in NM1 and \vec{J}_{s2} in NM2. Therefore, the spin torque $d\vec{S}_2 / dt$ can be expressed as follows in eq. (1.7).

$$\frac{d\vec{S}_2}{dt} - (\vec{J}_{s1} - \vec{J}_{s2}) = 0 \quad \dots (1.7)$$

\vec{S}_2 can be expressed as shown in eq. (1.8), using a (θ, ϕ) coordinate system.

$$\vec{S}_2 = \begin{pmatrix} \cos \phi \sin \theta \\ \sin \phi \sin \theta \\ \cos \theta \end{pmatrix} \quad \dots (1.8)$$

When \vec{S}_1 is fixed in the direction of $(0,0,1)$, the injected spin precesses around the z -axis in FM2 coordinate system, which is discussed in the next section on spin dynamics. If the phases and angles of precession of the electron spins are not the same (incoherent), the injected spin components completely cancel each other out. This difference can be understood as the spin-transfer torque. Then, equation (1.7) can be expressed as follows,

$$\frac{d\vec{S}_2}{dt} = g(\theta) \frac{I}{-e} \frac{\hbar}{2} \left[\begin{pmatrix} \cos \phi \sin \theta \\ \sin \phi \sin \theta \\ \cos \theta \end{pmatrix} - \begin{pmatrix} 0 \\ 0 \\ \cos \theta \end{pmatrix} \right] \quad \dots (1.9)$$

where I , e , and $\hbar/2$ are the applied current, the electron charge ($e > 0$), and the spin angular momentum of an electron, respectively. The factor $I/(-e)$ corresponds to the number of spins injected into FM2. Therefore, $I\hbar/2(-e)$ corresponds to the injected-spin angular momentum per unit time. $g(\theta)$ is the spin-transfer efficiency, which is different in CPP-GMR^[16] and MTJ^[18]. $g(\theta)$ is given by eq. (1.10).

$$g(\theta) = \begin{cases} \left[-4 + (P^{-1/2} + P^{1/2})^3 (3 + \cos \theta) / 4 \right]^{-1} & \text{(CPP-GMR)} \\ P / (1 + P^2 \cos \theta) & \text{(MTJ)} \end{cases} \quad \dots (1.10)$$

where P is the spin polarization (defined by eq. (1.3)).

We note the following outer product,

$$\vec{S}_1 \times (\vec{S}_2 \times \vec{S}_1) = \begin{pmatrix} 0 \\ 0 \\ 1 \end{pmatrix} \times \left[\begin{pmatrix} \cos\phi \sin\theta \\ \sin\phi \sin\theta \\ \cos\theta \end{pmatrix} \times \begin{pmatrix} 0 \\ 0 \\ 1 \end{pmatrix} \right] = \begin{pmatrix} \cos\phi \sin\theta \\ \sin\phi \sin\theta \\ 0 \end{pmatrix} \quad \dots (1.11)$$

Using eq. (1.11), equation (1.9) can be rewritten as,

$$\frac{d\vec{S}_2}{dt} = g(\theta) \frac{I}{-e} \frac{\hbar}{2} \vec{s}_2 \times (\vec{s}_1 \times \vec{s}_2) \quad \dots (1.12)$$

1.3 Spin Dynamics

The motion of spin is governed by the Landau-Lifshitz-Gilbert (LLG) equation^{[19],[20]}. In this section, the mathematical form of the LLG equation is derived and spin dynamics without damping and current is discussed.

For a constant value of the gyro magnetic ratio γ (<0), the angular momentum \vec{s} and magnetic moment \vec{m} have the following relationship,

$$\vec{m} = \gamma \vec{s} \quad \gamma = g \frac{\mu_0(-e)}{2m} \quad \dots (1.13)$$

where g , μ_0 , and m are the g factor, the magnetic permeability ($\mu_0 = 1.26 \times 10^{-6}$ H/m), and the mass of an electron, respectively. The total energy E required for \vec{m} to move in the effective field \vec{H}_{eff} can be written as (only Zeeman energy can be taken),

$$E = -\vec{m} \cdot \vec{H}_{\text{eff}} = -\gamma \vec{s} \cdot \vec{H}_{\text{eff}} \quad \dots (1.14)$$

To obtain the equation of motion of a spin, the Heisenberg equation can be used as,

$$\frac{d\vec{s}}{dt} = \frac{1}{i\hbar} [\vec{s}, E] \quad \dots (1.15)$$

Here, $[\vec{s}, E]$ represents the commutation relation of \vec{s} and E . Using the relation for the angular momentum (i.e., $[s_x, s_y] = s_x s_y - s_y s_x = i\hbar s_z$), eq. (1.15) can be written as,

$$\frac{d\vec{s}}{dt} = -\gamma (\vec{s} \times \vec{H}_{\text{eff}}) \quad \dots (1.16)$$

Since $\vec{S} = S\vec{s}$, eq. (1.17) follows naturally.

$$\frac{d\vec{S}}{dt} = -\gamma (\vec{S} \times \vec{H}_{\text{eff}}) \quad \dots (1.17)$$

Eq. (1.16) and (1.17) mean that the spin rotates around the effective magnetic field, and therefore, $\vec{S} \times \vec{H}_{\text{eff}}$ is referred to as the field torque.

If there is no energy dissipation, eqs. (1.16) and (1.17) are correct. However, the lowest energy point for a spin in a magnetic field is that at which it is oriented in the opposite direction to the vector of the magnetic field. Therefore, continuous precession is no longer stable when energy loss is considered. This phenomenological effect must be incorporated into eqs. (1.16) and (1.17). The equations thus become,

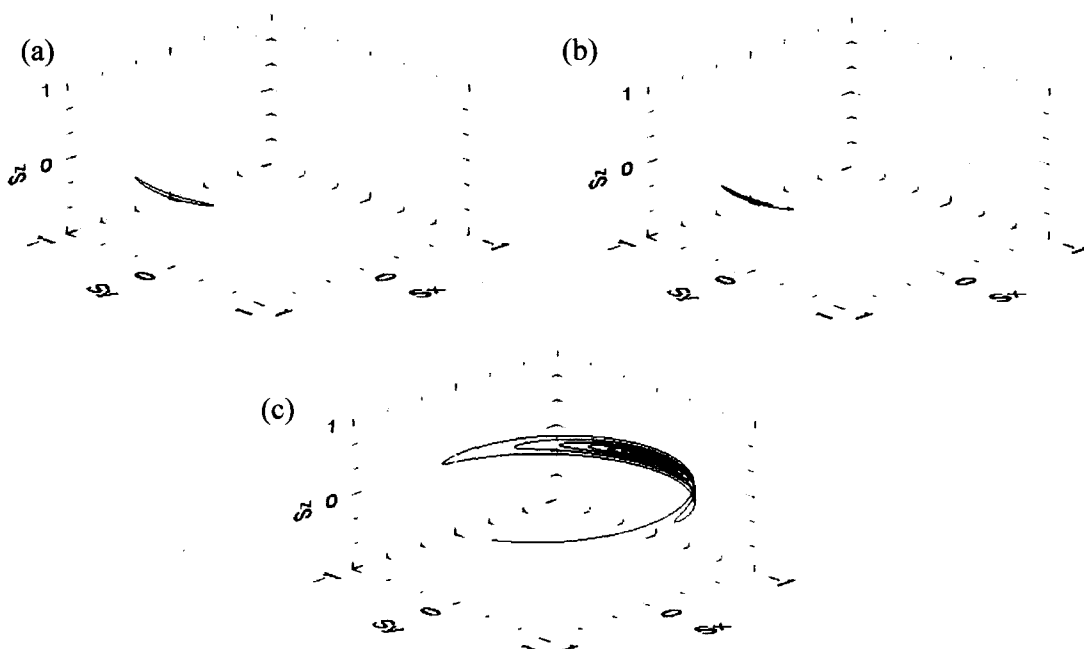


Fig. 5 Simulation results of spin dynamics without any currents. (a) $\alpha = 0$, (b) $\alpha = 0.01$, and (c) $\alpha = 0.01$ with an external magnetic field of 100 Oe applied along the x-axis. The spin precesses around the effective field, as shown in (a). However, it goes to the stable point when α has a finite value, as shown in (b). When there is an external magnetic field to overcome the coercive field, the direction of the spin is switched, as shown in (c).

$$\frac{d\vec{s}}{dt} = \gamma \vec{s} \times \vec{H}_{\text{eff}} + \alpha \vec{s} \times \frac{d\vec{s}}{dt} \quad \dots (1.18)$$

This is the so-called LLG equation, where α is the damping constant. Fig. 5 shows the simulated spin dynamics, as calculated using eq. (1.18). The damping constant α is 0 in Fig. 5 (a) and 0.01 in Fig. 5 (b). In Fig. 5 (a), the spin continues to rotate around the effective field when α is 0. However, the direction of spin becomes parallel with that of the effective field when α is not equal to 0, as shown in Fig. 5

(b). Here, the parameters used in the simulation were the coercive field $H_c = 50$ (Oe), the saturation magnetization (related to S) $M_s = 1000$ (emu/cc), and the initial direction of spin was almost in alignment with the x -axis. In Fig. 5 (c), the spin dynamics under the application of an external magnetic field to overcome the coercive field is shown. In the simulation, $H_{\text{ext}} = 100$ Oe was applied in the x -direction.

Eq. (1.18) expresses spin dynamics under only an effective magnetic field. When current is applied to the system, eq. (1.18) is no longer valid because of the presence of spin torque. From the above discussion, spin dynamics under a magnetic field and spin torque can be expressed using eqs. (1.12) and (1.18),

$$\frac{d\vec{S}_2}{dt} = \gamma\vec{S}_2 \times \vec{H}_{\text{eff}} + \alpha\vec{S}_2 \times \frac{d\vec{S}_2}{dt} + g(\theta)\frac{\hbar}{2-e} \vec{s}_2 \times (\vec{s}_1 \times \vec{s}_2) \cdot \cdot \cdot (1.19)$$

This equation is called the LLG-Slonczwski equation. The first, second, and third terms on the right hand side of eq. (1.19) are referred to as the field torque, damping torque, and spin torque, respectively. These torques are summarized in Fig. 6. If the spin torque is larger than the damping torque, the direction of spin can be switched.

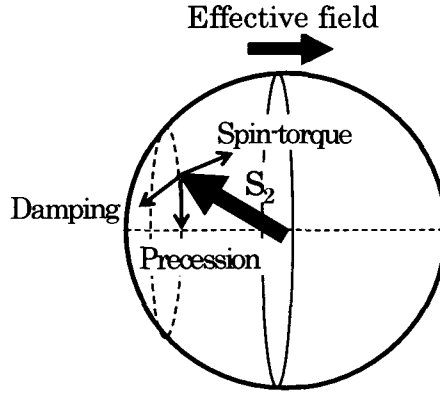


Fig. 6 A summary of torques applied to a spin. Spin torque can amplify (or attenuate) the angle of precession of spin, depending on the direction of current.

That is to say, the direction of spin can be controlled by not only a magnetic field but also a current. The condition to realize spin transfer switching is,

$$\alpha\gamma\vec{S}_2 \times (\vec{S}_2 \times \vec{H}_{\text{eff}}) < g(\theta)\frac{\hbar}{2-e} \vec{s}_2 \times (\vec{s}_1 \times \vec{s}_2) \cdot \cdot \cdot (1.20)$$

Therefore, the critical current I_{c0} for spin-torque switching is given by

$$I_{c0} = \frac{1}{g(\theta)} \frac{(-e)}{\hbar/2} \alpha\gamma S_2 H_{\text{eff}} \cdot \cdot \cdot (1.21)$$

The simulated results of the spin dynamics under a certain current, following eq. (1.19), are shown in Fig. 7. The applied current was +1.5 mA in Fig. 7 (a) and -1.5 mA in Fig. 7 (b). Here, the positive current is defined as electrons flowing from the free layer to the pinned layer, and the pinned layer is fixed in the (1, 0, 0) direction. The spin is switched to the opposite direction to the initial direction under a positive current, as shown in Fig. 7 (a). However, spin does not switch and settle at a stable point, as shown in Fig. 7 (b). In the simulation, a junction area of 100 nm \times 100 nm and a thickness of the free layer of 2 nm were assumed.

After the prediction of spin transfer effect, magnetization switching in GMR^{[21]-[24]} nano-pillars and MTJs^{[25],[26]} were observed.

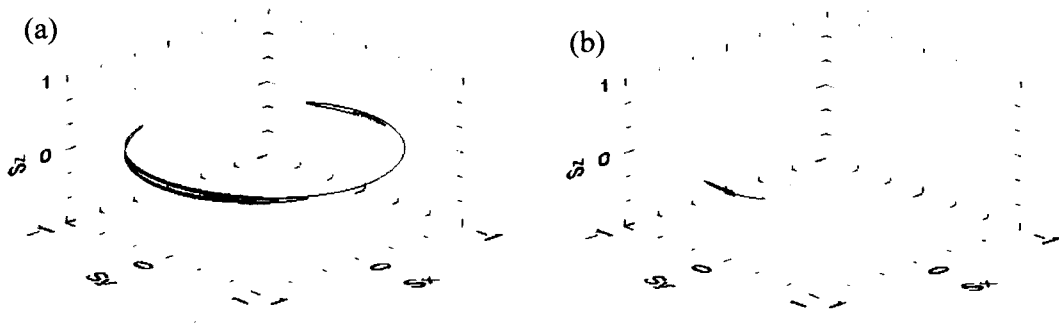


Fig. 7 Simulated spin dynamics under an applied current of (a) +1.5 mA and (b) -1.5 mA. The direction of spin is switched under a positive current (a); however, it is not changed under a negative current (b).

Thus far, spin dynamics in the presence of a magnetic field and a current have been introduced. Besides spin torque, there are other torques that exist under a finite current in an MTJ: field-like torque^{[27]-[29]} and voltage-induced torque^{[30]-[33]}. The latter has attracted much attention recently since it could possibly be used to realize magnetization switching with low energy consumption. However, these topics are not closely related to this work, and hence, I have not discussed them further here.

1.4 Spin Devices

In this section, spin devices, which utilize the advantages of spin, are described. Spin devices are very relevant to the key objectives of this study.

• Hard Disk Drives

MR effects (AMR, GMR, and TMR) have been already utilized in the reading heads of HDDs. As a result of the developments in MR devices and magnetic materials for storing, the areal density of HDDs has increased continuously. Fig. 8^[34] shows the development of the areal density of HDDs and dynamic random access memory (DRAM). The areal density in HDDs reached about 1 Tbit/inch² in 2010.

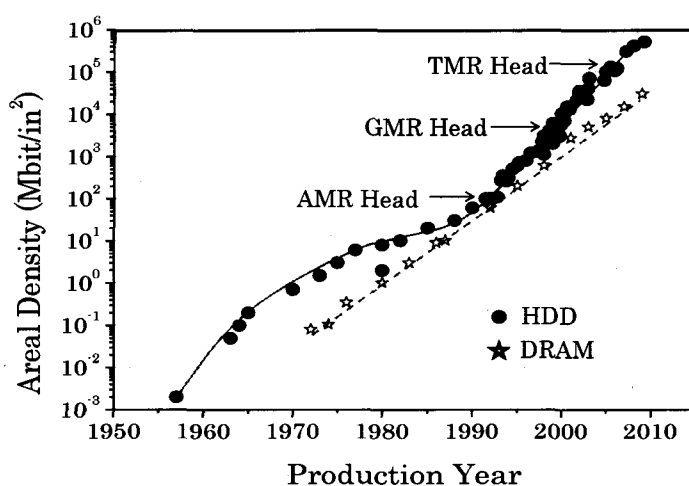


Fig. 8 The development of areal density in HDDs and DRAMs^[34]. The black dots show the development of HDDs. The discoveries of new MR effects have contributed to the increments in the areal density. For comparison, the developments of DRAM are shown with the white stars.

• Magnetic Random Access Memory

As MR devices have high and low resistance states, they can be used as a memory device. For example, the information “0” is stored as a low resistance state and “1” as high resistance. Memory using MR devices is called as Magnetic Random Access Memory (MRAM). Owing to its magnetic properties, MRAM is non-volatile memory, in which the information can be kept even if the power is turned off. In contrast, DRAM is volatile memory and it requires “Fresh operation” because

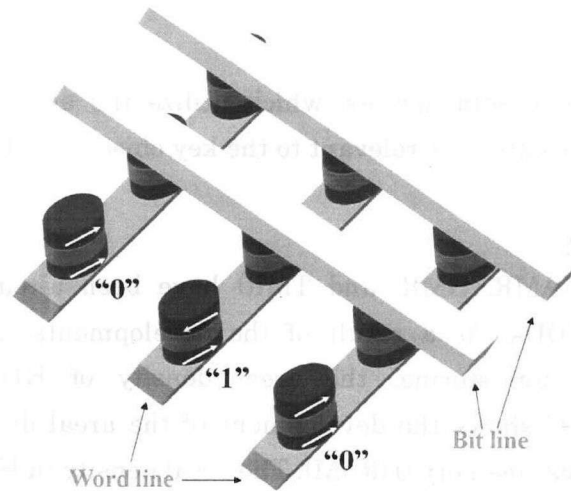


Fig. 9 A schematic diagram of MRAM. The magnetization configuration can be controlled by a combination of magnetic fields produced by passing currents through the bit and word lines. In the figure, the information “0” is stored as a low resistance state (parallel magnetization configuration) and “1” as high resistance (anti-parallel magnetization configuration).

information is stored using electric charges.

For use as memory devices, the electrical resistance of the memory needs to be changed through a suitable mechanism. In MRAM, rewriting the data corresponds to reversing the direction of the magnetization in the free layer. At present, there are two ways of doing this, one is by the application of an external magnetic field and the other is using spin-transfer torque^[35]. A schematic diagram of MRAM using magnetic field writing is shown in Fig. 9. In this writing method, the magnetization configuration (corresponding to stored information) can be controlled by a combination of magnetic fields produced by passing currents through the bit and word lines.

• Spin-Torque Oscillator (STO)

Spin-injection magnetization switching has been introduced in Section 1.3. The magnetization can be controlled by the direction of an applied current to the MR devices. The external magnetic field prevents the spin in P-state from being stable, while the current applied to the nano-pillar prevents the spin in the AP-state from being stable. In this situation, the P-state is no longer stable and the magnetization of the free layer goes into continuous precession. As explained in

Section 1.3, the frequency of precession is in the GHz range. If the magnetization of the free layer in an MR device has a frequency f_0 , the resistance of the device also oscillates with this frequency. As a result, the output voltage from an MTJ oscillates with a frequency f_0 under a certain bias current applied to the MTJ. By changing the external magnetic field, the output frequency can be changed. This construction is called a spin-torque oscillator (STO). It can be used as a small radio-frequency (RF) oscillator.

The STO was first reported using a GMR device by Kiselev^[36]. They used Co/Cu/Co nano-pillars with the dimensions $130 \times 70 \times 2 \text{ nm}^3$. Fig. 10 (a) shows their results for the STO. In the small current region, the resonant frequency does not shift significantly when the current amplitude is changed. However, when a higher current is applied, the RF output rapidly increases and resonant frequencies become lower. This change in the resonant frequencies was explained by a change in the precession orbit: if precession with a large angle is induced, then the frequency becomes smaller. The maximum amplitude in their experiments was several tens of picowatts. They also showed the phase diagram as functions of external magnetic fields and applied current, as shown in Fig. 10 (b). If the negative magnetic field is large, the preferred state of the system is the P-state. Under a certain current and weak negative magnetic field, the AP-state is preferred due to spin-transfer

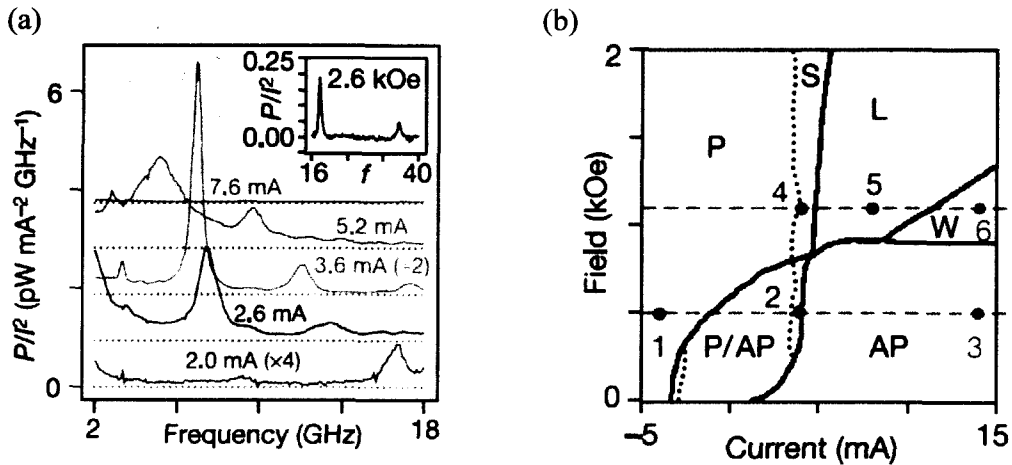


Fig. 10 (a) RF power density spectra normalized by the square of the injected current into the GMR nano-pillar. The external magnetic field was 2.0 kOe and the injected currents were 2 mA, 2.6, 3.6, and 7.6 from bottom to top.

(b) A phase diagram observed in a GMR nano-pillar. The state “W” indicates a state with resistance between P and AP states with only small RF output.

Both (a) and (b) were reported by Kiselev et. al.^[36]

switching. In the region “L” (large current and large magnetic field), it goes into continuous precession. They also found a region “W” in which the spectra have large line widths. This area was explained using micro-magnetic simulations, in which chaotic spin motion was observed.

After the first report of an STO by Kiselev, many approaches to increase the output amplitude of an MR device were suggested[37]. One example is the phase lock phenomenon, which uses two point nano-contacts^{[38],[39]}. Another example was demonstrated by Rippard^{[40],[41]}, who applied a perpendicular magnetic field and obtained quite a large Q-value of 18000.

An STO using an MgO-based MTJ was first demonstrated by Deac^[42]. As a result of the large MR ratio in the MgO-based MTJ, a large emission was obtained. They used a CoFeB/MgO/CoFeB MTJ with dimensions of $70 \times 160 \times 2 \text{ nm}^3$. The output spectrum as a function of frequency is shown in Fig. 1.11 (a). The maximum amplitude obtained was about $0.14 \text{ } \mu\text{W}$, which is 10 times larger than the first values reported using GMR. Fig. 1.11 (b) shows the phase diagram of the RF output with respect to applied current and external magnetic field. Compared to GMR devices, the spectra are complicated, which may be caused by domain formation in

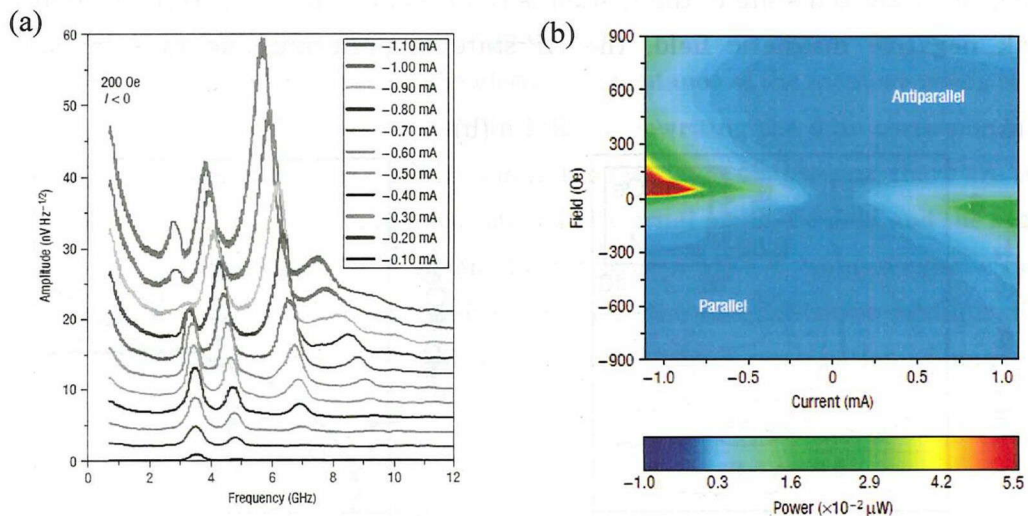


Fig. 11 (a) RF power density spectra normalized by the square of the injected current into the MTJ nano-pillar. The external magnetic field is 200 Oe and the injected current is changed from -0.1 mA -1.1 mA.

(b) Current-field phase diagram observed in an MTJ nano-pillar. The asymmetrical behavior of the bias current due to the spin torque is shown.

Both (a) and (b) were reported by Deac *et. al.*^[42]

the nano-pillar. The phase diagram is related to RF amplification, as discussed in Section 3.3.

Spin Transistors

Spin transistors are new types of devices, in which the attractive properties of spin, such as the MR effect and high frequency, are exploited. As described above in regard to MRAM, spin can be used as non-volatile information storage. Since the direction of spin can be easily controlled by magnetic fields and currents, spin can also be used for reconfigurable logic devices. Of course, established MR devices can also be used for logic circuits, but they are passive devices, and hence, they do not recover attenuated signals through amplification and do not have sufficient fan-out. Therefore, three-terminal active devices have attractive features that have motivated their further development.

Spin transistors can be applied for non-volatile logic circuits. In volatile circuits, power must always be supplied to the system to maintain information because storage is accomplished using electrical charges. However, in non-volatile logic circuits using spin transistors, a power supply is not required because magnetization configurations are used for storage. Power is only needed when operations are carried out in the non-volatile logic circuits. Therefore, spin transistors can be employed in low-power-consumption devices. Furthermore, spin transistors can contribute to high circuit integration since flip-flops (used for storage in normal circuits) are not needed owing to the logical-operation and storage functionalities of spin transistors.

Owing to the different concepts and principles of the various spin transistors proposed and demonstrated until now, I cannot refer to the

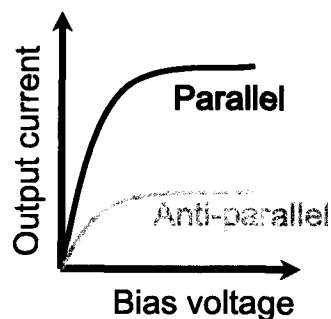


Fig. 12 Output current as a function of bias voltage. Black and gray curves indicate the output characteristics of parallel and anti-parallel configurations, respectively.

characteristics of spin transistors in a general manner. However, it can be said that they all contain ferromagnetic materials and change their output characteristics by manipulating magnetic configurations. In Fig. 12, the general output characteristics as a function of the bias voltage are shown. In the figure, the black and gray curves indicate the output current in parallel and anti-parallel configurations, respectively. The output current is larger in the parallel than anti-parallel configuration due to the MR effects. The change in output current γ_{MC} is defined by eq. (1.22).

$$\gamma_{MC} = \frac{I_P - I_{AP}}{I_{AP}} \times 100[\%] \quad \dots (1.22)$$

Here, I_P and I_{AP} are the current in the parallel and anti-parallel configurations under a certain bias voltage. γ_{MC} is the magneto-current ratio and is an important parameter for evaluating spin transistors.

Many types of spin transistors have been proposed, such as the spin-diffusion transistor^[43], spin-valve transistor^[44], Datta-Das type spin-field-effect transistor (spin-FET)^[45], magnetic bipolar spin transistor^[46], spin metal-oxide-semiconductor field-effect transistor (spin-MOSFET)^[47], spin single-electron transistor^[48], and spin-torque transistor^[49]. These spin transistors can be separated into two types. In the first type, the amplification properties of the semiconductor are combined with spin-dependent transport. The other devices use the amplification properties of the spin system and spin-dependent transport.

Fig. 13 shows representative examples of the two types of spin transistors. In the spin-MOSFET, the gate voltage controls the Schottky barrier width at the source/channel interface. In the spin-FET, the direction of the transported spin in

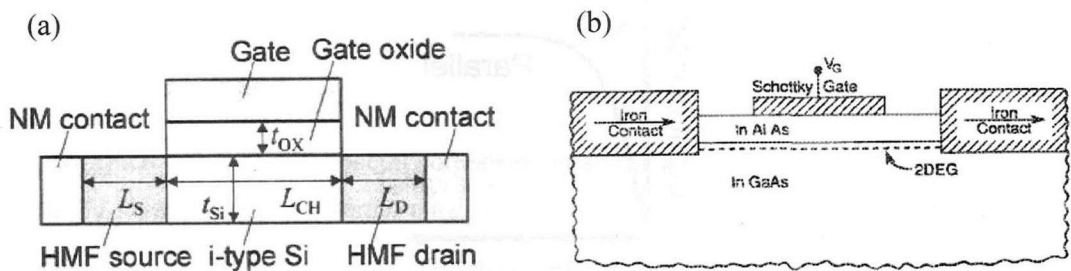


Fig. 13 Schematic of the structures of (a) a spin-MOSFET^[47] and (b) a spin-FET^[45].

Gate voltage can control the conductance in a spin-MOSFET, however, it acts to transport spin directly in a spin-FET.

the channel can be controlled by the gate voltage using Rashba effect. These spin transistors have attractive features: for example, good scalability in the spin-MOSFET.

In addition to spin transistors, an MgO-based MTJ can be applied in magnetic logic circuits, such as a non-volatile full adder^[50], non-volatile field programmable gate arrays (FPGAs)^{[51]-[53]}, magnetically coupled spin-torque devices^[54] and three terminal devices^{[55],[56]}. Furthermore, new MTJ-based applications, e.g., RF amplifiers^[57], have been proposed and demonstrated.

1.5 Objectives of this Study

As discussed in the previous section on spin devices, new types of devices using new concepts, structures, and operating principles have been both proposed and demonstrated. However, the power amplification property, which is necessary for Boolean logic operation, has not yet been realized in any spin transistors at room temperature for a variety of reasons, including the difficulties of controlling the spin in the semiconductor, the low efficiency of spin injection into Si at room temperature, and the complicated structure of such devices.

To achieve active devices in spintronics, giant TMR ratio is very powerful. An image of feedback system in MR devices is shown in Fig. 14. When magnetization configuration in MTJs changes, conductance change occurs due to MR effect. Then, additional torques, such as magnetic field and/or spin torque, appear because of change in current passing through MTJs. In a feedback system, these additional torques are again applied to the MR devices as feedback forces. If these feedback forces are too small, the feedback system is incomplete, hence, active devices cannot be realized. However, feedback forces, in MgO-based MTJs, can become larger due to its large TMR ratio. To realize spintronic active devices, (e.g., spin torque oscillator) the feedback force should be again applied to the first MTJ. And for the information propagation, feedback force should be applied to other cells to control next MTJs.

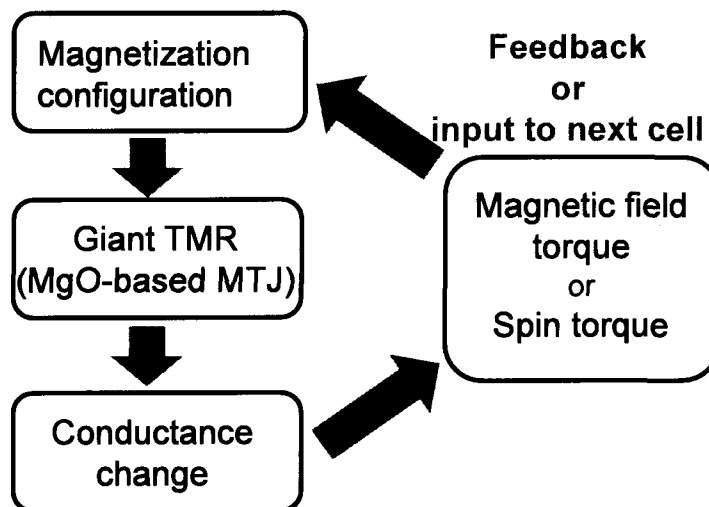


Fig. 14 An image of feedback system using MTJs. To realize active devices with MTJs, large feedback forces are required because it is applied to MTJs. To transfer information, feedback force should be applied to next cells to control next MTJs.

In this study, MgO-based MTJs are employed to investigate its amplification phenomena for spintronic active devices. Magnetization direction can be controlled by three methods; magnetic field, spin torque and voltage induced magnetization reversal. The final one has recently developed and the effect was small at the time when this study was started. The first one is simple way, however, still no report of amplification. The second one, as described below is investigated of the amplification, however, no report of amplification. The brief overview of each section is described below.

(Sec. 2) Under the background described above, I firstly propose the concepts of spin transistor, one is driven by current-induced magnetic field and another is driven by spin torque. Then, the characteristics, such as power gain, current gain and fan-out, in both spin transistors are introduced by theoretical approach. The motivation of experiments on current-field driven spin transistor is finally described.

(Sec. 4.1) To evaluate the amplification properties of the device, CoFeB / MgO / CoFeB MTJs were prepared by micro-fabrication on MTJs, which were fabricated using magnetron sputtering. In addition to confirming the switching behavior by a current-induced magnetic field, the dependency of the amplification properties on the bias voltage was measured. To achieve this, the bias dependence of the resistance in an MTJ was measured. To clarify the design principles of the device, the results of theoretical calculations and experimental measurements were compared.

(Sec. 4.2) Only sufficient power amplification in the device is not adequate to state that the device can be used as a basic component in non-volatile logic devices. Therefore, the fan-out value was evaluated, which indicates the number of MTJs driven by the output from a single MTJ. In addition, the non-volatility is an important parameter for the device. To evaluate this, the thermal stability factor is introduced.

(Sec. 4.3) In order to show the new functionalities of MgO-based MTJs, the RF amplification properties are investigated. First, the static external magnetic field dependencies of the RF amplification properties are described. Then, a comparison between the experimental results and those of a simple macro-spin model simulation are shown. Finally, the design principles needed to enhance the RF amplification property are described.

Chapter 2 Device scaling (theoretical derivation)

In this chapter, the device scaling in the magnetic field driven and spin torque driven spin transistors are introduced by theoretical approach. To compare the device scaling law in each spin transistors, the characteristics of each spin transistors are discussed.

2.1 Concept of the current-field driven spin transistors

The concept of the proposed device, driven by a current-induced magnetic field (current-field) is shown Fig. 15. The basic structure, which is surrounded by a dotted line-frame in Fig. 15, is composed of a magnetic tunnel junction (MTJ-A) and an electrically-isolated metallic wire-A which is used to switch the free layer of the MTJ-A by producing a magnetic field. It is very similar to that of the conventional field-driven MRAM, however, the concept and the architecture are very different. Current application to the metallic wire-A generates a magnetic field and switches the free layer magnetization direction in the MTJ-A. Because of the resistance change of the MTJ, the power consumed in the wire -B, which is cascaded to the MTJ-A, is changed. This may affect the magnetization switching in the MTJ-B. If

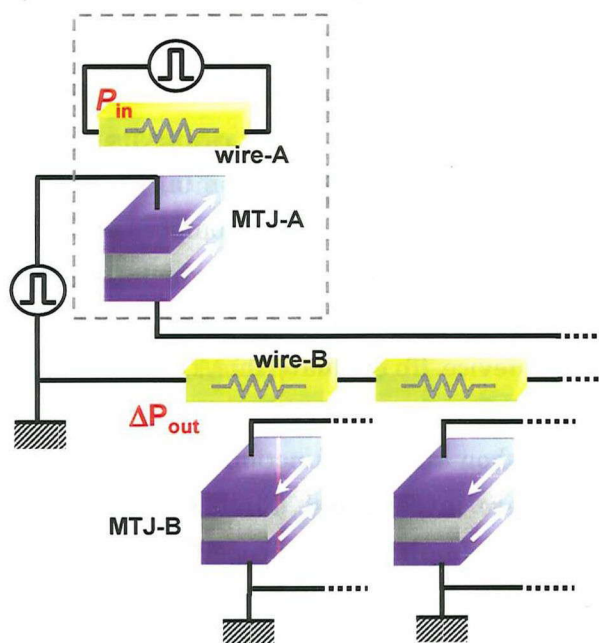


Fig. 15 A schematic diagram of the electrical circuit of the current-field driven spin transistor.

the change in the output power (ΔP_{out}) and the output current (ΔI_{out}) between the parallel and anti-parallel magnetization configurations in the MTJ-A is larger than the input power (P_{in}) and the input current (I_{in}) consumed by the pulse application to the wire-A, this device can drive the cascaded basic structure and may function as a logic circuit. Because of this power amplification property, we call this device as a “spin transistor”. Here, we define the power gain and the current gain as,

$$G_{power} \equiv \frac{\Delta P_{out}}{P_{in}} = \frac{P_{AP} - P_P}{P_{pulse}} \quad \dots (2.1)$$

$$G_{current} \equiv \frac{\Delta I_{out}}{I_{in}} = \frac{I_{AP} - I_P}{I_{pulse}} \quad \dots (2.2)$$

The image of power and current gain are shown in Fig. 16 (a) and (b), respectively. The power gain means that a signal, which posse information, is amplified by getting energy from an external source (indicated as P_{supply} in the figure). Due to the power amplification, the information can be transferred. Another amplification factor is current gain. Current gain is one of the most important

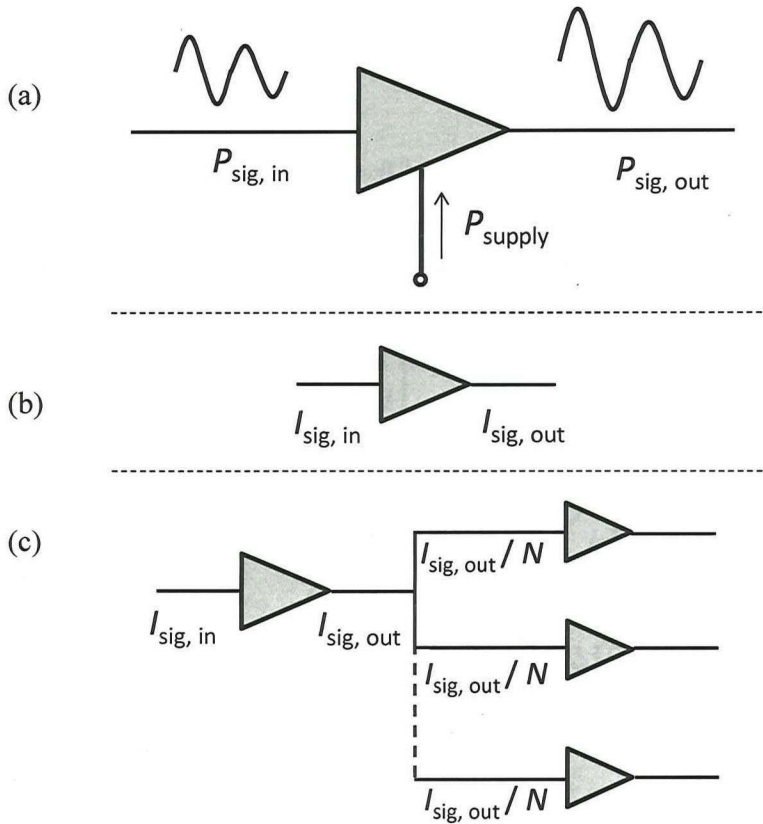


Fig. 16 The images of (a) power gain, (b) current gain and (c) fan-out

parameters because proposed spin transistors are driven by current. Current gain means input current is amplified in output current. Besides power and current gain, fan-out value is index parameter in the Boolean circuit. The image of fan-out value is shown in Fig. 16(c). It represents that the number (N), which can be controlled by an output from an MTJ. In the case of proposed spin transistors, output current ($I_{\text{sig, out}}$) from an MTJ is divided by N , and current $I_{\text{sig, out}}/N$ controls next MTJs, which is cascaded to the first MTJ.

2.2 Scaling of current-field driven spin transistors

Now I derive the scaling of the current-field driven spin transistor. The scaling model is shown in Fig. 17. When a current I_w is applied to a CPW whose width is w , a generated magnetic field around CPW H_w is,

$$H_w \approx \frac{I_w}{2w}. \quad \dots (2.3)$$

In order to induce magnetization switching, $H_w \geq H_c$ should be satisfied. Here, H_c is a coercive field of ferromagnetic materials in a free layer, empirically described as^[62],

$$H_c \approx \xi \frac{a}{L} M_s + H_0 \quad \dots (2.4)$$

where a , L , ξ , M_s and H_0 are the thickness of free layer, a length of junction pillar of an MTJ, a proportional parameter, a saturation magnetization and the relative coercive field of ferromagnetic material, respectively. Eq. (3.2) can be separated into two parts as,

$$H_c = \begin{cases} H_0 & (L \text{ is large}) \\ \xi \frac{a}{L} M & (L \text{ is small}) \end{cases} \quad \dots (2.5)$$

Then, the aspect ratio of MTJ k is introduced, i.e., $w = kL$. Substituting eq. (2.5) to eq. (2.3),

$$I_w = \begin{cases} 2kH_0L & \propto L^1 \quad (L \text{ is large}) \\ 2k\xi aM & \propto L^0 \quad (L \text{ is small}) \end{cases} \quad \dots (2.6)$$

Eq. (2.6) describes the current for induction of magnetization switching. Further, a resistance of CPW (R_w) is,

$$R_w = \rho \frac{k'w}{tw} = \rho \frac{k'}{t} \quad \dots (2.7)$$

Where, ρ and k' are the resistivity of CPW material, aspect ratio between width and length, resistivity. Therefore, the input power that is consumed by the wire-A is calculated as,

$$P_w = I_w^2 R_w = \begin{cases} (2kH_0L)^2 \rho \frac{k'}{t} \propto L^2 \quad (L \text{ is large}) \\ (2k\xi aM)^2 \rho \frac{k'}{t} \propto L^0 \quad (L \text{ is small}) \end{cases} \quad \dots (2.8)$$

For the detail expression, eq. (2.3) will be rewritten as,

$$H_w \approx \frac{I_w}{2w + \pi(a + 2d + t)} \quad \dots (2.9)$$

Where, t and d are a thickness of CPW and a distance between CPW and free layer, respectively. Eq. (2.3) and (2.8) should be rewritten as,

$$I_w = \left(\xi \frac{a}{L} M + H_0 \right) (2w + \pi(a + 2d + t)) \quad \dots (2.10)$$

$$P_w = I_w^2 R_w = \left\{ \left(\xi \frac{a}{L} M + H_0 \right) (2w + \pi(a + 2d + t)) \right\}^2 \rho \frac{k'}{t} \quad \dots (2.11)$$

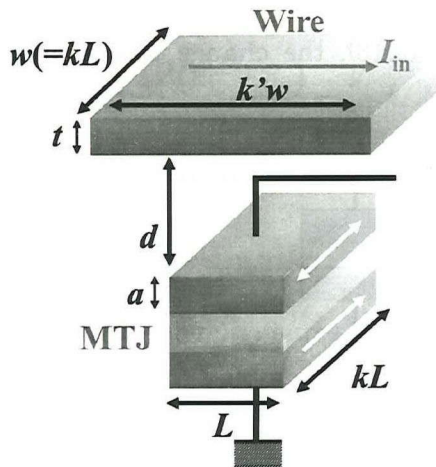


Fig. 17 A schematic diagram of the scaling model (current-field driven spin transistor).

Next, I consider about an output power and an output current from an MTJ. An output power and an output current depends on states of an MTJ (parallel or anti-parallel) and connections of an MTJ and a CPW (series connection or parallel connection).

(1) Series connection case

In the series connection, a constant voltage source is used shown in Fig. 18. The applied voltage to wire-B V_L is,

$$V_{L(P, AP)} = \frac{R_L}{R_{P, AP} + R_L} V \quad \dots (2.12)$$

Where, R_L and V are resistance of wire-B and a voltage of constant voltage source. Then, change in the output power ΔP_{out} is described as (2.13).

$$\begin{aligned} \Delta P_{out} &= \frac{V_{L(P)}^2}{R_L} - \frac{V_{L(AP)}^2}{R_L} = V^2 R_L \left(\left(\frac{1}{R_P + R_L} \right)^2 - \left(\frac{1}{R_{AP} + R_L} \right)^2 \right) \\ &= V^2 R_L \left(\frac{(R_{AP} + R_L)^2 - (R_P + R_L)^2}{(R_P + R_L)^2 (R_{AP} + R_L)^2} \right) = V^2 R_L \left(\frac{R_{AP}^2 - R_P^2 + 2R_L(R_{AP} - R_P)}{(R_P + R_L)^2 (R_{AP} + R_L)^2} \right) \quad \dots (2.13) \\ &= V^2 R_L \left(\frac{(R_{AP} + R_P) + 2R_L}{(R_P + R_L)^2 (R_{AP} + R_L)^2} \right) (R_{AP} - R_P) \end{aligned}$$

Here, I introduce an average resistance of MTJ R_T as,

$$R_T = \frac{R_P + R_{AP}}{2} \quad \dots (2.14)$$

Substituting eq. (2.14) to (2.13), the change in the output power (ΔP_{out}) can be derived as,

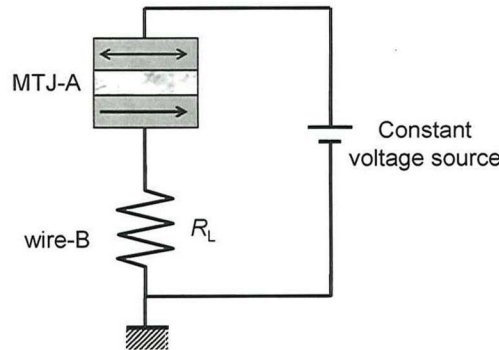


Fig. 18 A schematic image of the series connection of MTJ-A and wire-B with a constant voltage source.

$$\Delta P_{\text{out}} \approx \frac{2V^2 R_L}{(R_T + R_L)^3} (R_{\text{AP}} - R_P) \quad \dots (2.15)$$

In order to know the maximum output, I differentiate eq. (3.15) with respect to R_L , i.e.,

$$\frac{\partial}{\partial R_L} (\Delta P_{\text{out}}) \propto \frac{\partial}{\partial R_L} \frac{R_L}{(R_T + R_L)^3} = \frac{R_T - 2R_L}{(R_T + R_L)^4} \quad \dots (2.16)$$

To satisfy $\frac{\partial}{\partial R_L} (\Delta P_{\text{out}}) = 0$, $R_L = \frac{R_T}{2}$ should be satisfied. In this condition,

$$\Delta P_{\text{out}}(\text{max}) = \frac{8V^2}{27R_T} \text{MR}^* = \frac{8V^2}{27RA} kL^2 \text{MR}^* \propto L^2 \quad \dots (2.17)$$

Here, MR^* is defined as,

$$\text{MR}^* = \frac{2(R_{\text{AP}} - R_P)}{(R_{\text{AP}} + R_P)} \quad \dots (2.18)$$

Output current can be calculated in the similar manner with output power,

$$\Delta I_{\text{out}} = \frac{V}{R_P + R_L} - \frac{V}{R_{\text{AP}} + R_L} \approx \frac{V(R_{\text{AP}} - R_P)}{(R_T + R_L)^2} \quad \dots (2.19)$$

Eq. (2.19) trivially shows that ΔI_{out} has the maximum when $R_L = 0$ (i.e., short circuit). Then,

$$\Delta I_{\text{out}}(\text{max}) = \frac{V(R_{\text{AP}} - R_P)}{R_T^2} = \frac{V}{RA} kL^2 \text{MR}^* \propto L^2 \quad \dots (2.20)$$

(2) Parallel connection case

Next, I consider parallel connection of MTJ-A and wire-B (shown in Fig. 19). In parallel connections, a constant current source is assumed. An applied voltage to wire-B (V) is described as,

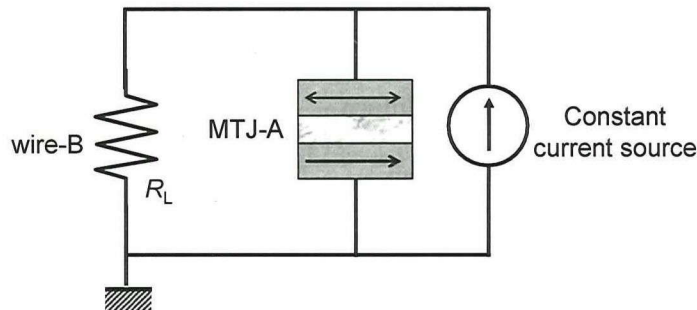


Fig. 19 A schematic image of the parallel connection of MTJ-A and wire-B with a constant current source.

$$V = \frac{R_{P,AP}R_L}{R_{P,AP} + R_L} I \quad \dots (2.21)$$

Hence, a difference in an output power ΔP_{out} is,

$$\begin{aligned} \Delta P_{out} &= \frac{V_{AP}^2}{R_L} - \frac{V_P^2}{R_L} = I^2 R_L \left(\left(\frac{R_{AP}}{R_{AP} + R_L} \right)^2 - \left(\frac{R_P}{R_P + R_L} \right)^2 \right) \\ &= I^2 R_L \left(\frac{(R_P + R_L)^2 R_{AP}^2 - (R_{AP} + R_L)^2 R_P^2}{(R_{AP} + R_L)^2 (R_P + R_L)^2} \right) \quad \dots (2.22) \\ &= I^2 R_L^2 \frac{R_L (R_{AP} + R_P) + 2R_P R_{AP}}{(R_{AP} + R_L)^2 (R_P + R_L)^2} (R_{AP} - R_P) \end{aligned}$$

Here,

$$R_{//} = \frac{R_P R_{AP}}{R_{AP} + R_P} \quad \dots (2.23)$$

Finally,

$$\Delta P_{out} = I^2 R_L^2 \frac{(R_{AP} + R_P)^2 (R_L + 2R_{//})}{2(R_{AP} + R_L)^2 (R_P + R_L)^2} MR^* \quad \dots (2.24)$$

Using same manner with the series connection, the condition to obtain the maximum output power is $R_L = 2R_T$. Under this condition, the output power can be approximated as,

$$\Delta P_{out} \approx \frac{8}{27} I^2 R_T MR^* \quad \dots (2.25)$$

To make eq. (2.25) simply using eq. (2.17),

$$\Delta P_{out} = \frac{2}{3} \frac{V^2}{R_T} MR^* = \frac{2}{3} \frac{V^2}{R_A} kL^2 MR^* \propto L^2 \quad \dots (2.26)$$

Next, ΔI_{out} is estimated as,

$$\begin{aligned} \Delta I_{out} &= \frac{V_{AP}}{R_L} - \frac{V_P}{R_L} = I \left(\left(\frac{R_{AP}}{R_{AP} + R_L} \right) - \left(\frac{R_P}{R_P + R_L} \right) \right) \\ &\approx I \frac{1}{(R_T + R_L)^2} (R_{AP}(R_P + R_L) - R_P(R_{AP} + R_L)) = I \frac{R_L \Delta R}{(R_T + R_L)^2} \quad \dots (2.27) \end{aligned}$$

when $R_L = R_T$, ΔI_{out} reaches the maximum,

$$\Delta I_{out}(\max) = \frac{1}{4} I MR^* \quad \dots (2.28)$$

Using eq. (2.21),

$$\Delta I_{\text{out}}(\text{max}) = \frac{V}{2R_{\text{T}}} MR^* = \frac{V}{2RA} kL^2 MR^* \propto L^2 \quad \dots (2.29)$$

Comparing eq. (2.20) and (2.29), larger output current is obtained in a series connection.

A theoretical input and output power (current) were calculated and optimized in the above discussion. Next, I would like to discuss the theoretical power and current gain in this device. At first, I show a tendency of power and current gain against length L . From eq. (2.17) (for series connection) and eq. (2.26) (for parallel connection), power gain (G_{power}) in the device has a relation,

$$G_{\text{power}} = \frac{\Delta P_{\text{out}}}{P_{\text{in}}} \propto \begin{cases} L^0 & (\text{L is large}) \\ L^2 & (\text{L is small}) \end{cases} \quad \dots (2.30)$$

Eq. (2.30) indicates power gain is proportional to L^2 when junction size is small. And it becomes constant (not related with L) with increasing L . For the current gain (G_{current}), tendencies can easily be obtained from eq. (2.20) and (2.29),

$$G_{\text{current}} = \frac{\Delta I_{\text{out}}}{I_{\text{in}}} = \begin{cases} L^1 & (\text{L is large}) \\ L^2 & (\text{L is small}) \end{cases} \quad \dots (2.31)$$

Thus, current gain is proportional to L^2 same as power gain when junction size is small, however, is proportional to L when junction size becomes larger. For the detail expression of power gain in parallel connection, from eq. (2.11) and (2.16),

$$G_{\text{power}} = \frac{\frac{2}{3} \frac{V^2}{RA} kL^2 MR^*}{\left\{ \left(\xi \frac{a}{L} M + H_0 \right) (2w + \pi(a + 2d + t)) \right\}^2 \rho \frac{k'}{t}} \quad \dots (2.32)$$

From eq. (2.10) and (2.20), the current gain in series connection is,

$$G_{\text{current}} = \frac{\frac{V}{RA} kL^2 MR^*}{\left(\xi \frac{a}{L} M + H_0 \right) (2w + \pi(a + 2d + t))} \quad \dots (2.33)$$

In the above discussion, the model is somewhat ideal, however, parasitic series resistances, which are connected to an MTJ and a CPW cannot be ignored in the real device. Therefore, I introduce an influences of parasitic resistances on power gain and current gain hereafter. The scaling model is shown in Fig. 20.

Parasitic resistances are connected to an MTJ ($R_{S,T}$) and a CPW ($R_{W,T}$). In this model, the power gain (eq. (2.32)) and the current gain (eq. (3.33)) can be transformed to,

$$\begin{aligned}
 G_{\text{power}} &= \frac{\frac{2}{3} \frac{V_T^2}{R_T + R_{S,T}} \frac{\Delta R}{R_T + R_{S,T}}}{\left\{ \left(\xi \frac{a}{b} M + H_0 \right) (2w + \pi(a + 2d + t)) \right\}^2 \left(\rho \frac{k'}{t} + R_{S,w} \right)} \\
 &= \frac{\frac{2}{3} \frac{V_T^2}{R_T \left(1 + \frac{R_{S,T}}{R_T} \right)} \frac{\Delta R}{R_T \left(1 + \frac{R_{S,T}}{R_T} \right)}}{\left\{ \left(\xi \frac{a}{b} M + H_0 \right) (2w + \pi(a + 2d + t)) \right\}^2 \rho \frac{k'}{t} \left(1 + \frac{R_{S,w}}{\rho \frac{k'}{t}} \right)} \\
 &= \frac{\frac{2}{3} \frac{V_T^2}{RA} kL^2 MR^*}{\left\{ \left(\xi \frac{a}{b} M + H_0 \right) (2w + \pi(a + 2d + t)) \right\}^2 \rho \frac{k'}{t}} \left(1 + \frac{R_{S,T}}{RA} kL^2 \right)^{-2} \left(1 + \frac{R_{S,w}}{\rho \frac{k'}{t}} \right)^{-1} \quad \dots (2.34)
 \end{aligned}$$

The power gain based on eq. (2.34) is plotted in black curve in Fig. 23 (page 43). In the same manner, current gain with parasitic resistance is described as,

$$G_{\text{current}} = \frac{\frac{V}{RA} kL^2 MR^*}{\left(\xi \frac{a}{L} M + H_0 \right) (2w + \pi(a + 2d + t))} \left(1 + \frac{R_{S,T}}{RA} 4b^2 \right)^{-2} \quad \dots (2.35)$$

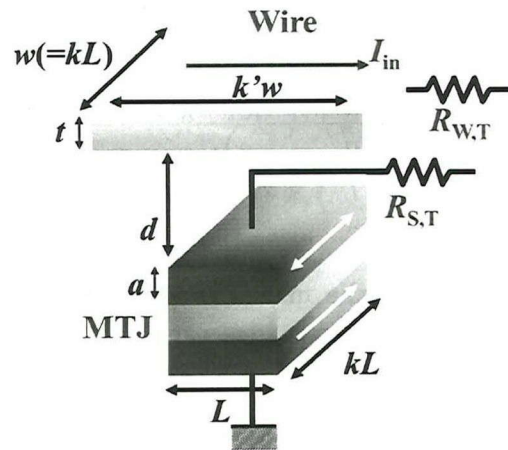


Fig. 20 A schematic diagram of the scaling model with series parasitic resistances. 38

To estimate the fan-out value, MTJ-A and n-wire-Bs are assumed to be connected in series, as shown in Fig. 21. The maximum voltage V without breakdown of the MTJ-A in this circuit is described as follows,

$$V = (1 + nR_L/R_T)V_{MTJ} \quad \dots (2.36)$$

In the case of load resistance, the output current can be described as,

$$\Delta I_{out} = \frac{V}{R_P + R_L} - \frac{V}{R_{AP} + R_L} \approx \frac{V_{MTJ}}{R_T(1 + nR_L/R_T)^2} MR^* \quad \dots (2.37)$$

From eq. (2.36) and (2.37), we conclude that,

$$\Delta I_{out} = \frac{V_{MTJ}}{R_T(1 + nR_L/R_T)} MR^* \quad \dots (2.38)$$

Through substitution of eq. (2.10) and (2.37) in the definition of current gain (i.e. eq. (2.2)), we obtain the expression for the current gain as,

$$G_{current} = \frac{V_{MTJ}}{(2w + \pi(a + 2d + t))I_w \times R_T} MR^* \quad \dots (2.40)$$

The maximum fan-out value is estimated by assuming $\Delta I_{out} = 2I_{in}$ as described in the manuscript. In this condition, the fan-out value is described as follows:

$$\text{Fan-out} = \frac{R_T}{R_L} \left(\frac{\Delta I_{out}}{2I_{in}} - 1 \right) = \frac{R_T}{R_L} \left(\frac{G_{current}}{2} - 1 \right) \quad \dots (2.41)$$

Finally, to substitute (2.41) to (2.42), fan-out value is given as,

$$\text{Fan-out} = \frac{R_T}{R_L} \left(\frac{V_{MTJ} \times MR^*}{2 \times (2w + \pi(a + 2d + t))I_w \times R_T} - 1 \right) \quad \dots (2.42)$$

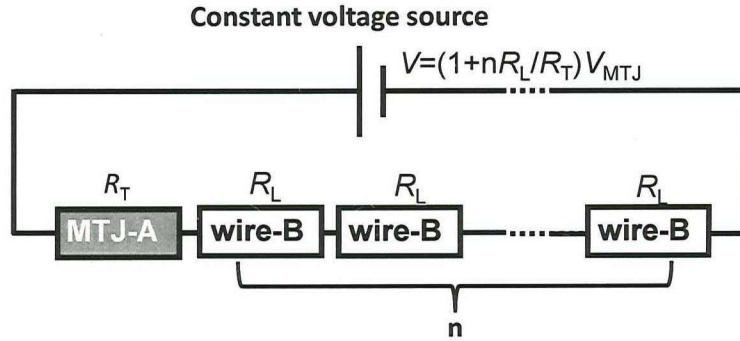


Fig. 21 A schematic diagram of the electrical circuit for fan-out estimation.

From eq. (2.42), the fan-out value becomes larger as the ratio of resistance of MTJ and load (CPW) is increased. This is because constant voltage is shared with an MTJ and load resistances in series connection. The fan-out value based on eq. (2.42) is plotted in the black curve in Fig. 24 (page 45).

2.3 Concept of the spin torque driven spin transistor

The device concept of spin torque driven spin transistor is described in this section. A schematic diagram of spin transistor is shown in Fig. 21(a). The structure is similar with three terminal device, proposed in ref. 55. The left electrode is for the writing (controlling magnetization direction), consisting of GMR device. Due to low resistance in GMR device, the input power can be small. The bottom and right electrodes are for the reading. The output power can be larger due to high MR ratio in MTJ structure. Input current switches magnetization of current injection area, then, magnetization switching spreads whole free layer under application of current. Finally, magnetization reversal can be realized. The behavior of magnetization of the free layer under current application is shown in Fig. 21(b).

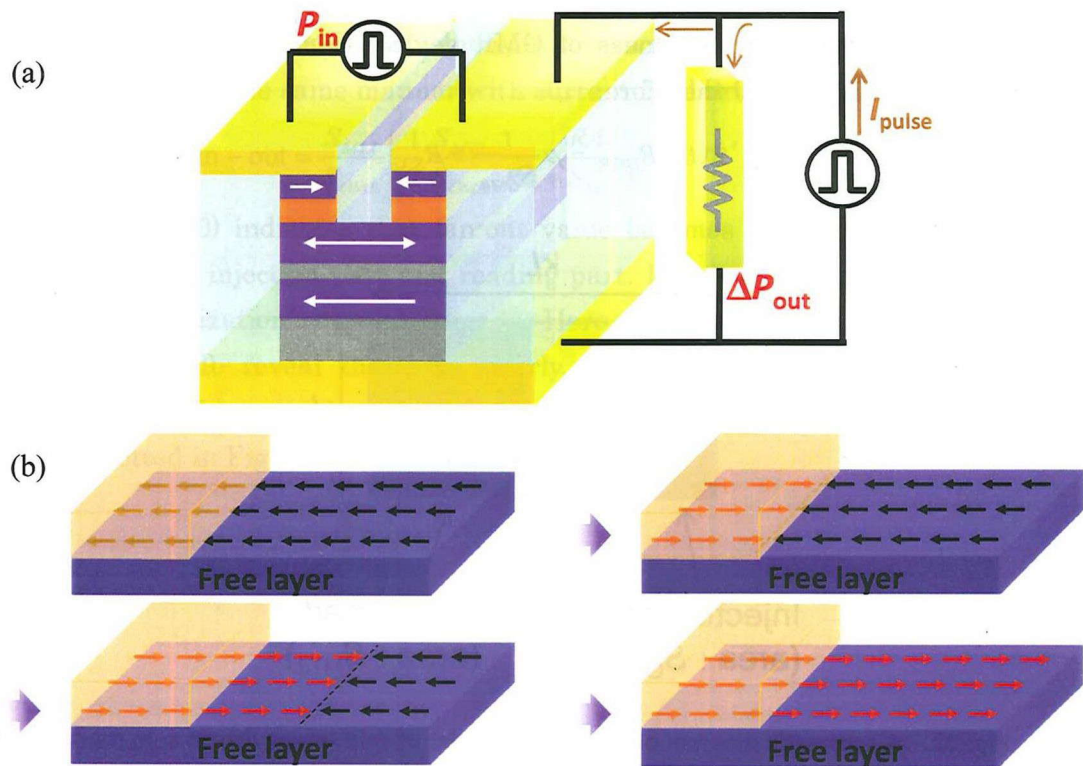


Fig. 21 (a) A schematic diagram of the device concept of spin torque driven spin transistor.

Writing : spin torque in GMR part, Reading : MTJ

(b) An image of magnetization switching in the free layer. Spin polarized current is injected into a part of free layer, inducing magnetization reversal under the electrode. The domain wall forms and spreads under application of current. Finally, magnetization reversal occurs whole free layer.

2.4 Scaling of spin torque driven spin transistor

In this section, the scaling of the spin torque driven spin transistor is introduced. The input current can be written as,

$$I_{in} = I_c \times S_{GMR} \quad \dots (2.42)$$

Here, I_c is the critical current for magnetization switching and S_{GMR} is the area of GMR device. Using the resistance of GMR (R_{GMR}), the input power can be written as eq. (2.39)

$$P_{in} = (I_c \times S_{GMR})^2 \times R_{GMR} \quad \dots (2.43)$$

If R_{GMR} does not have series parasitic resistance, R_{GMR} is simply,

$$R_{GMR} = \rho \frac{t_{GMR}}{S_{GMR}} \quad \dots (2.44)$$

Where t_{GMR} is the total thickness of GMR device. Usually, a GMR device has parasitic resistance ($R_{S,G}$) therefore,

$$R_{GMR} = \rho \frac{t}{S_{GMR}} + R_{S,G} \quad \dots (2.45)$$

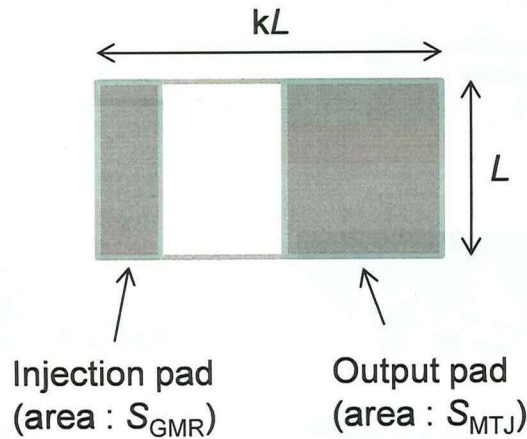


Fig. 22 A schematic diagram of the scaling model of spin torque driven spin transistor.

The output power and current are same as eq. (2.26) and (2.20), respectively. From eq. (2.26) and (2.43), power gain in spin torque driven type spin transistor is,

$$G_{power} = \frac{\frac{2}{3} \frac{V_{MTJ}^2}{RA} S_{MTJ} MR^*}{(S_{GMR} J_c)^2 \frac{RA}{S_{MTJ}}} \quad \dots (2.46)$$

If the series resistance is introduced,

$$G_{\text{power}} = \frac{2 V_T^2}{3 RA} \frac{S_{MTJ} MR^*}{(S_{GMR} J_c)^2} \left(\frac{RA}{S_{GMR}} + R_{W,S} \right)^{-1} \left(1 + \frac{R_{S,T}}{RA} S_{MTJ} \right)^{-2} \quad \dots (2.47)$$

The power gain based on (2.47) is plotted in the next section. The current gain can be described from eq. (2.20) and (2.42),

$$G_{\text{current}} = \frac{\frac{V_{MTJ}}{RA} S_{MTJ} MR^*}{S_{GMR} J_c} \quad \dots (2.48)$$

$$G_{\text{current}} = \frac{\frac{V_{MTJ}}{RA} S_{MTJ} MR^* \left(1 + \frac{R_{S,T}}{RA} bc \right)^{-2}}{S_{GMR} J_c} \quad \dots (2.49)$$

Fan-out value in spin torque driven type spin transistor is consistent with current gain. The fan-out value in the spin torque driven spin transistor is derived from eq. (2.41), (in the same manner with current-field driven spin transistor),

$$\text{Fan-out} = \frac{S_{MTJ}}{S_{GMR}} \left(\frac{1}{2} \frac{S_{MTJ}}{S_{GMR}} \frac{RA}{RA + S_{MTJ} R_{S,T}} MR^* - 1 \right) \quad \dots (2.50)$$

Eq. (2.50) indicates that fan-out value becomes larger by increasing the ratio of areas of injection part and reading part. However, the ratio is limited by how far magnetization reversal spreads. Here the ratio of 3 is assumed for the device scaling. To reveal the ratio clearly, micro-magnetic simulation must be performed. The fan-out value in spin torque driven spin transistor according to eq. (2.50) is plotted in Fig. 24 in the next section.

2.5 Comparison of characteristics of spin transistors

The theoretical power gain with parasitic series resistances as a function of MTJ size (L) are shown in Fig. 23. The black and red curves represent the power gain in current-field driven spin transistor and spin torque driven spin transistor based on eq. (2.32) and eq. (2.47), respectively. The current-field driven spin transistor has a peak around $1 \mu\text{m}$ as indicated in the black curve. The peak position is determined by the ratio of resistance of MTJ (i.e., RA product) and series resistance. Although the maximum power gain is around 100 in current-field driven spin transistor, it reaches to 500 at small size in spin torque driven spin transistor. The power gain in spin torque driven spin transistor is almost constant when L is smaller than 100 nm . The reason is that as size becomes smaller, the input power can be smaller since required current for switching is proportional to the size and the output power also becomes smaller because resistance becomes higher. So, the input and output power are cancelled each other. From Fig. 23, spin torque driven spin transistor is superior in scaling of power gain.

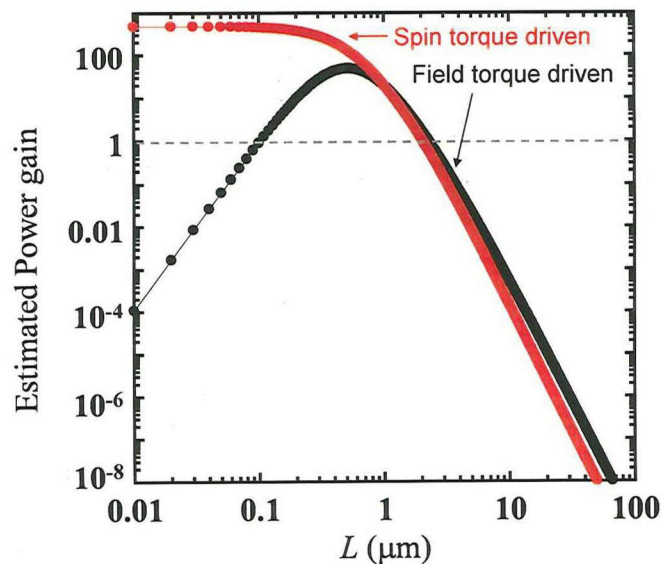


Fig. 23 The theoretical power gains as function of MTJ feature size (L). Black (red) curve shows the estimated power gain in the current-field (spin torque) driven spin transistor. Parameters used in the calculations are as follows.

Fig. 24 shows the theoretical fan-out values in both type of spin transistors as a function of device feature size according to eq. (2.41) and (2.50). Black and red curves show the current-field and spin torque driven spin transistors, respectively. From the red curve, fan-out value in spin torque type is difficult to obtain in all size (the maximum value is almost 2). However, the fan-out value in current-field driven spin transistor achieves about 8 at maximum despite that the scaling window is very small (limited to 0.1 – 1 μm).

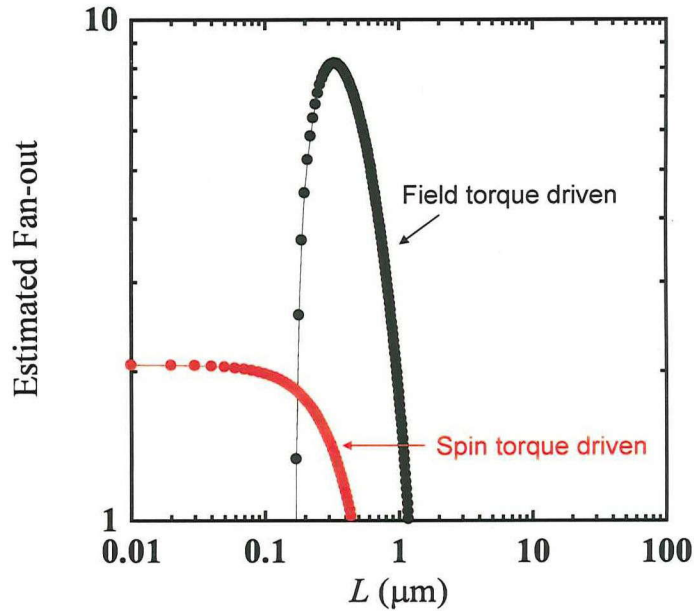


Fig. 24 The theoretical fan-out values as function of MTJ feature size (L). Black (red) curve shows the estimated power gain in the current-field (spin torque) driven spin transistor. Parameters used in the calculations are same as Fig. 23.

The parameters used in Fig. 23 and 24 are as follows.

- MR ratio : $\text{MR} = 100\%$ ($\text{MR}^* = 2/3$)
- Saturation magnetization : $M = 1$ [T] ($= 8 \times 10^5$ [A/m])
- Applied voltage to an MTJ : $V_{\text{MTJ}} = 0.4$ [V]
- Aspect ratio of an MTJ : $k = 3$
- Aspect ratio of CPW (length / width) : $k' = 10$
- Thickness of free layer : $a = 3$ [nm]
- A proportional parameter of coercive field : $\xi = 0.3$
- A relative coercive field : $H_0 = 3$ [Oe] ($= 2.4 \times 10^2$ [A/m])

- Distance between CPW and free layer : $d = 0.16$ [μm]
- Thickness of CPW : $t = 0.1$ [μm]
- The resistivity of CPW : $\rho = 5 \times 10^{-7}$ [Ωm]
- Series resistance to MTJ : $R_{S,T} = 10$ [Ω]
- Series resistance to CPW : $R_{S,W} = 5$ [Ω]
- The ratio of area of MTJ and GMR : $S_{MTJ} / S_{GMR} = 3$
- Critical current for CIMS : $J_c = 1 \times 10^6$ [A/cm^2]

To conclude this chapter, the larger power gain can be obtained in spin torque driven spin transistor. The power gain is the important parameter for information transferring. However, the fan-out value is more important parameter in Boolean operation. Therefore, I choose to conduct experiments (chapter 4) the current-field spin transistor, in which the fan-out value is easier to be obtained.

x

Chapter 3 Experimental method

In this chapter, the experimental methods are shown. The main topics of this chapter consists of three topics, which are film fabrication, micro-fabrication and measurements methods.

3.1 Film fabrication

The thin films used in this study were fabricated by a magnetron sputtering (Canon ANELVA C7100) in the National Institute of Advanced Industrial Science and Technology (AIST). Fig. 25 shows a schematic diagram of the thin film. Film stack was fabricated on thermally oxide Si substrate. Ta / CuN / Ta / CuN / Ta layers were used as bottom electrodes. Using double CuN layers, we can reduce the sheet resistance of bottom electrode. PtMn / CoFe / Ru / CoFeB layers were called as “Synthetic anti-ferromagnetic pinned layer (SyAF)”. Here, PtMn / CoFe layers are for the spin-valve structure. Thanks to the coupling between PtMn and CoFe, it can work as pinned layer. CoFe and CoFeB are anti-ferromagnetically coupled by adjusting thickness of Ru. The magnetizations of these layers are opposite direction. By this, the stray magnetic fields applied to free layers can be cancelled. MgO layer is used as an insulator. Free layer consists of CoFeB or CoFeB/Ru/NiFe, depending

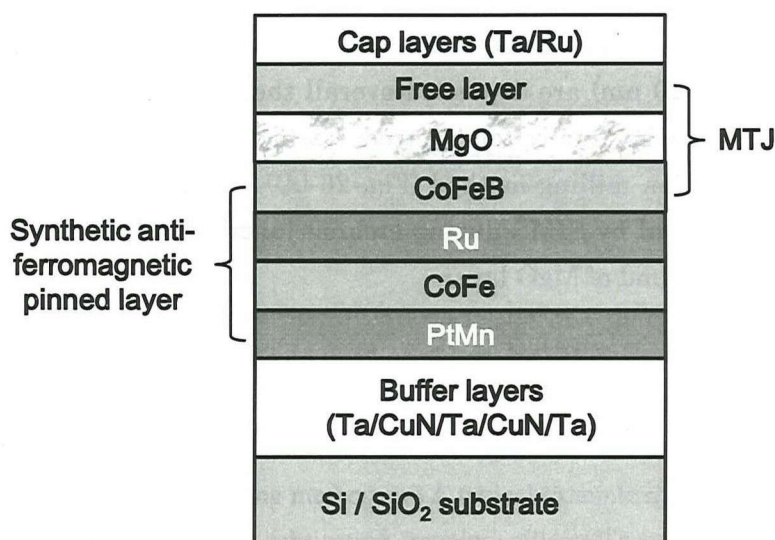


Fig. 25 A schematic diagram of cross-sectional view of sputtered film. MTJ consists of the structure CoFeB/MgO/free layer. CoFeB or CoFeB/Ru/NiFe stacks are used as free layer, depending on experiments.

on the experiments. Ta / Ru layers are used as cap layers.

After film fabrication, MR and RA products were measured by the current in-plane tunneling (CIPT) method^[58]. This method is convenient to know the MR and RA because we don't need micro-fabrication and we can directly measure MR and RA values after film fabrication.

3.2 Micro-fabrication

To measure electric properties, micro-fabrication has to be performed to films. In this study, micro-fabrication was done by electron beam (EB) lithography (ELS-3700, Elionix), Ar ion milling (Hakuto) with secondary ion mass spectrometry (SIMS) system and magnetron sputtering for depositing SiO₂ insulating layer and EB evaporation system (i-Quick, Canon ANELVA) for making electrodes. The procedure of micro-fabrication is largely separated into two parts as shown below.

(I) Junction pillar with electrodes

The detail procedure of micro-fabrication of junction pillars is shown in Fig. 26. Firstly, bottom electrodes are patterning (not shown in Fig. 26). Second, etching masks (resist) are patterned into junction shapes using EB lithography (Fig. 26 (a)). Third, cap layers, free layer and MgO layer are etched by Ar ion milling except for the parts covered by etching masks (Fig, 26 (b)). Fourth, a SiO₂ interlayer insulating layer (10 to 20 nm) are deposited overall the sample (Fig. 26 (c)). After lifting-off the etching masks, finally, top electrodes, which consist of Cr / Au (80 nm), are deposited using Ar ion milling method (Fig. 26 (d)). Fig. 26 (e) shows a typical example of detected signal by SIMS during etching junction pillar. The etching is stopped at the middle or end of MgO layer.

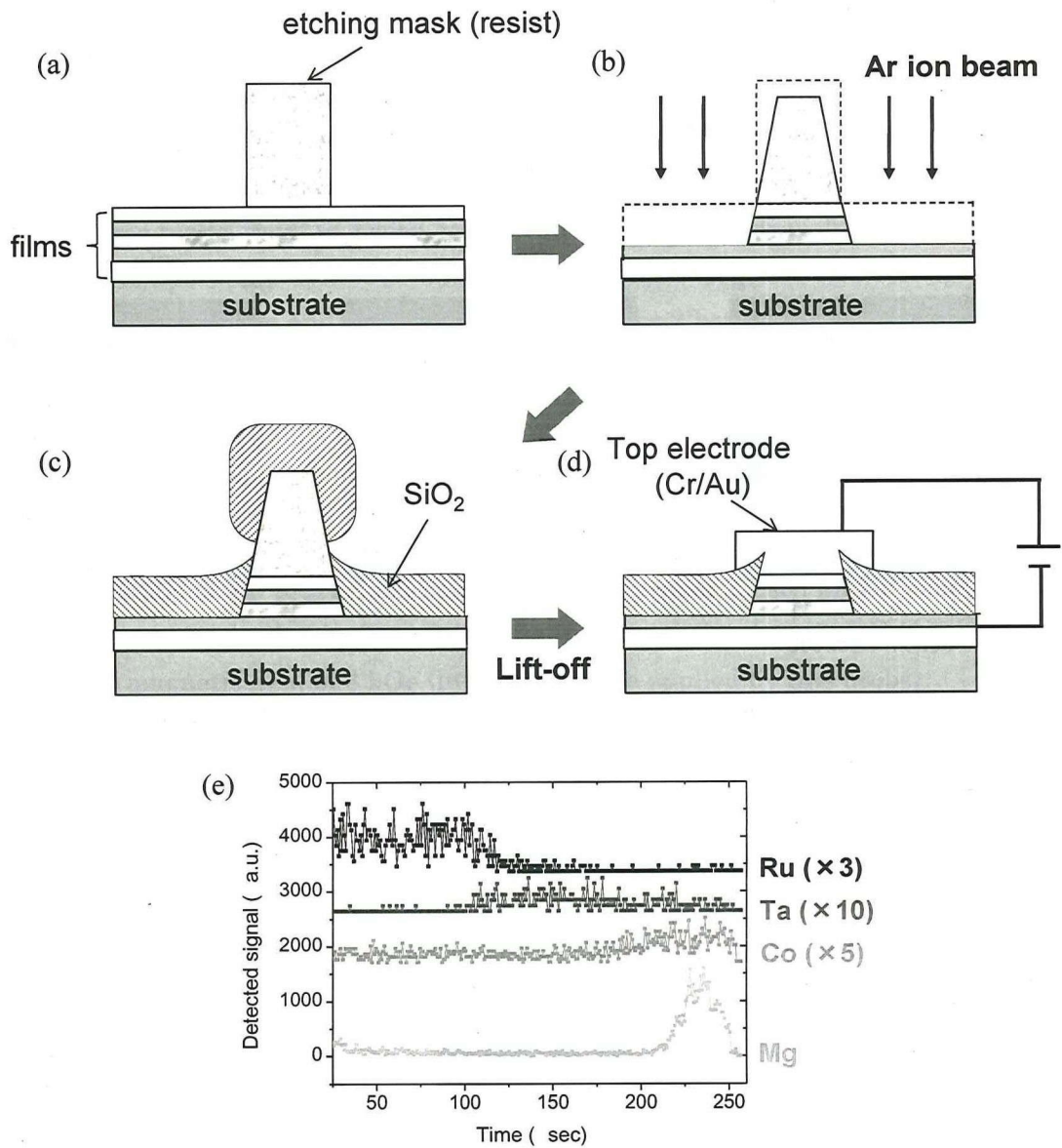


Fig. 26 The procedure of micro-fabrication for junction pillars with electrodes. (a) An etching mask is patterned into junction shapes by EB lithography. (b) Using patterned etching mask, a part of the film is etched by Ar ion milling. (c) A SiO₂ interlayer insulating layer is deposited. (d) After lifting-off the etching mask, top electrode is deposited by Ar ion milling method. (e) A typical example of detected signal by SIMS during etching films for fabricating junction pillars. The signals are enhanced and shifted for clarity. The etching is stopped at the middle or end of etching of MgO layer.

(II) CPW

After fabricating junction pillars, a SiO₂ insulating layer of 60 nm is deposited on the sample except for probe contact area, as shown in Fig. 27 (b). Then, CPWs are fabricated by lift-off method as shown in Fig. 27 (c). At this time, the signal line of CPW must be aligned just over the junction pillars in order to apply

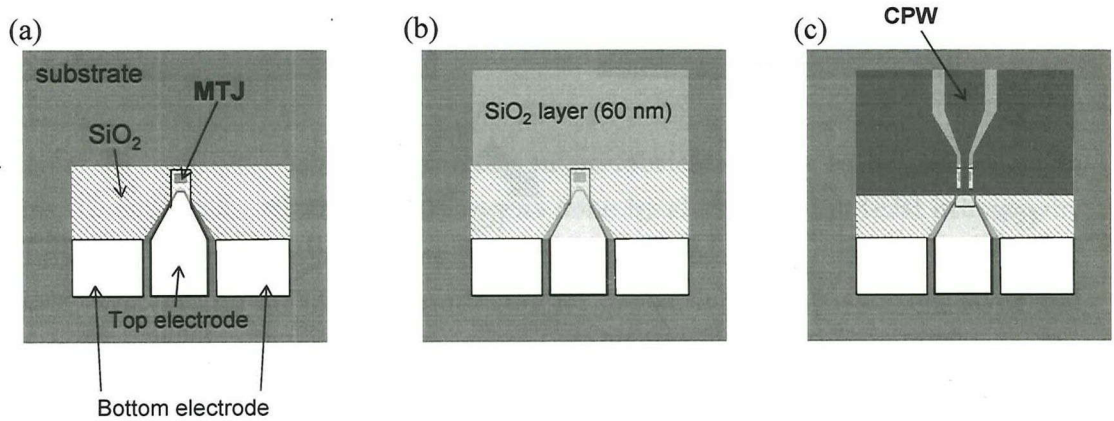


Fig. 27 The micro-fabrication process for CPWs. (a) After micro-fabrication of junction pillar. (b) A SiO₂ insulating layer of 60 nm is deposited all over the samples, excepting for contact area. (c) CPWs are deposited on the SiO₂ insulating layer. The signal line of CPW is aligned just over the junction pillars to apply magnetic fields to the free layer of MTJ.

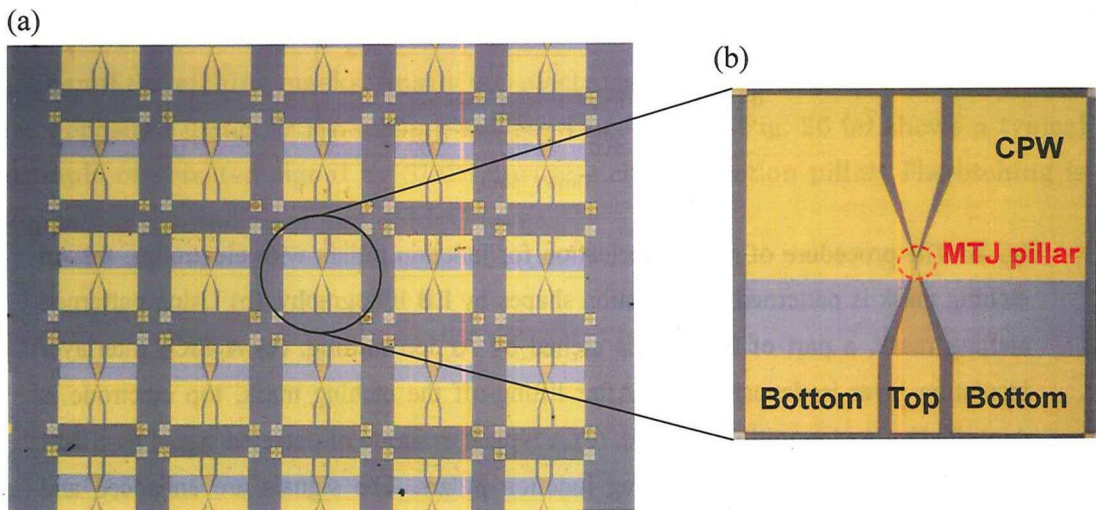


Fig. 28 Optical microscope images of sample. (a) over view (b) close-up of one MTJ and one CPW.

magnetic fields to the free layer of MTJ. The width of CPW depends on the length of the long axis of MTJ (e.g. the width of CPW is $2\ \mu\text{m}$ when MTJ size is $1\ \mu\text{m} \times 2\ \mu\text{m}$). Optical microscopic images of sample are shown in Fig. 28.

After finishing micro-fabrication, samples are annealed in a furnace with applying magnetic field in order to fix the direction of pinned layer^{[59]-[61]}. The annealed temperature is about 300 degrees Celsius degree. The strength of a magnetic field is 6 kOe and samples are annealed for 2 hours.

3.3 Measurements

In this section, the details of measurements methods are shown. Basically, to measure MR or RF property required magnetic prober. I used an RF prober with electro-magneto provided by Toei Scientific Industrial Co., Ltd (東栄科学産業). The maximum magnetic field of 3 kOe (in-plane) can be applied by this prober.

3.3.1 MR measurements

The measurements circuit for MR measurements is shown in Fig. 29. A lock-in amplifier (SR 830, Stanford Research Systems) is used as a voltage supply and a detector. The series resistance of $1\ \text{k}\Omega$ is connected in series with an MTJ. Usually, resistance of an MTJ is measured by two terminals method.

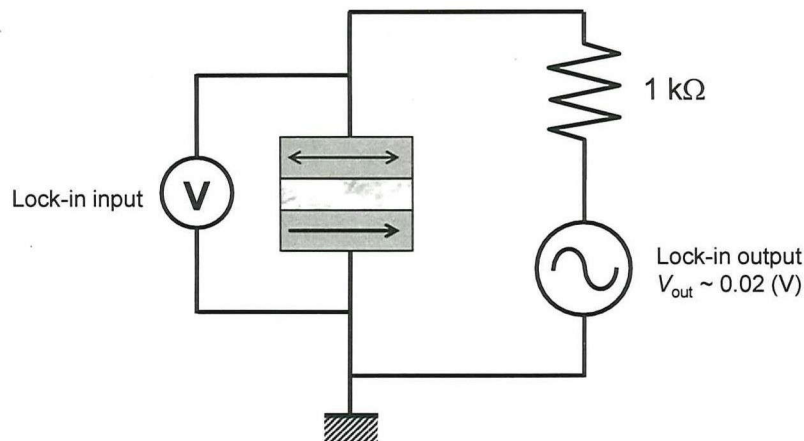


Fig. 29 Measurement circuit for MR measurements. The resistance of the MTJ is monitoring with changing external magnetic field.

3.3.2 Pulse switching measurements

The measurement circuit for magnetic field pulse switching measurements is shown in Fig. 30. A sourcemeter (ke2400, KEITHLEY) is used for monitoring resistance of an MTJ. A pulse generator (AFG 3252, Tektronics) is used for application of voltage to a CPW for generating pulsed magnetic field. Due to this field, magnetization switching in the free layer in an MTJ occurs and resistance of an MTJ changes. An oscilloscope (DSO 3202, Agilent) is used as a monitor of the amplitude of the applied pulses.

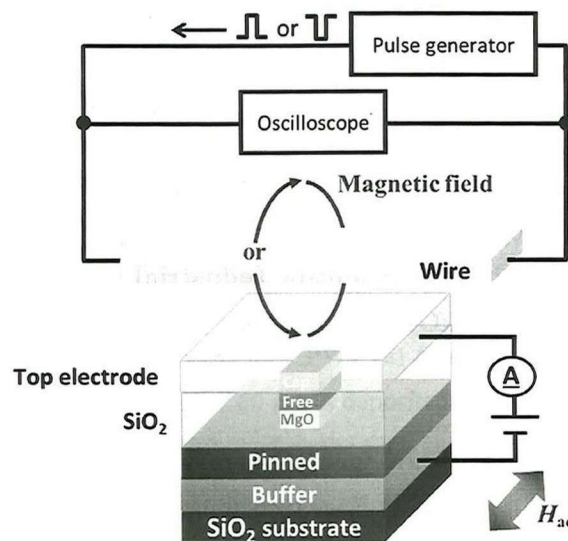


Fig. 30 Measurement circuit for MR measurements. From a pulse generator, pulses are applied to CPW wire and the pulses are detected by an oscilloscope. During pulse applications, the resistance of MTJ is monitored by a sourcemeter. H_{ac} represents an assisting ac magnetic field, that will be introduced in Sec. 3.2.

3.3.3 RF amplification measurements

Fig. 31 shows a measurement circuit for RF amplification, which is discussed in Sec. 3.3. From the port-1 of vector network analyzer (VNA, E8364B Agilent), RF voltage (V_{in}) is applied to a CPW. A bias current is applied to an MTJ through the bias-Tee using a sourcemeter. The RF output from an MTJ (V_{out}) is detected at port-2 of VNA. Using a VNA, S_{21} parameter, which is defined as $S_{21} = V_{out} / V_{in}$, can be obtained.

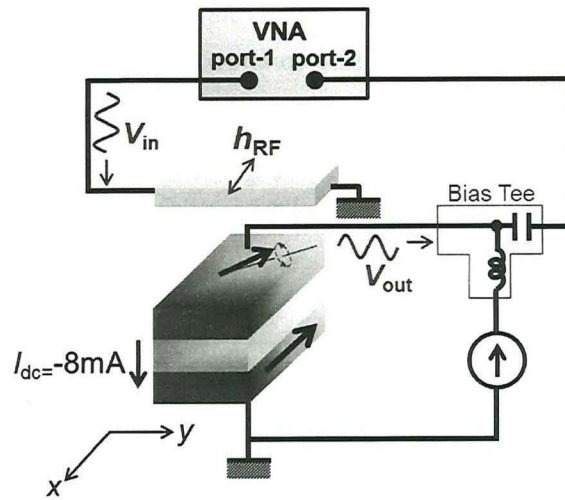


Fig. 31 Measurement circuit for RF amplification measurements. From the port-1 of VNA, V_{in} is applied to a CPW, generating RF magnetic field around the CPW. Bias voltage is applied to an MTJ by sourcemeter. The RF output from an MTJ can be detected as S_{21} parameter. A bias Tee is used as a separator of DC and RF signal.

Chapter 4 Results and Discussion

In this chapter, I would like to show and discuss the experimental results. The chapter is largely separated into 2 sections. One is pulse amplification and another is RF amplification.

4.1 Power amplification

In this section, the results of power gain measurements are shown. Before discussing main results of the power gain, basic physical properties of MTJ are described. The free layer of the first sample is CoFeB with the thickness of 2 nm. From current in-plane tunneling (CIPT) measurements, the RA value and MR ratio were evaluated to be $3.7 \Omega\mu\text{m}^2$ and 129%, respectively.

Typical MR curve of MTJ with CoFeB (2 nm) free layer after micro-fabrication is shown in Fig. 32. The area of junction pillar is $0.5 \times 2 \mu\text{m}^2$ and the width of CPW is $2 \mu\text{m}$. Fig. 32 indicates MR ratio is 24%, which is 5 times smaller than found from the results of CIPT measurements, because of an influence of a parasitic series resistance. Fig. 33 shows the junction size dependence of resistance of MTJs. The horizontal axis is inverse of junction area. From the linear fitting of the junction area, the parasitic series resistance (intercept) and actual RA (gradient) were evaluated to be around 10Ω and $4.4 \Omega\mu\text{m}^2$, respectively, in my device.

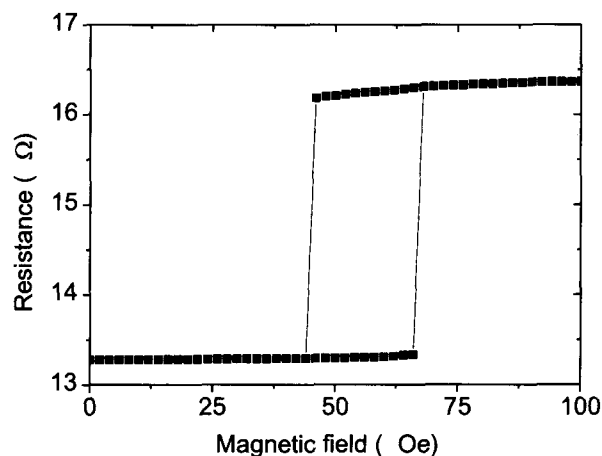


Fig. 32 MR curve measured using the circuit shown in Fig. 29. The junction size is $0.5 \times 2 \mu\text{m}^2$. The obtained MR ratio is about 24%. The obtained MR value is much smaller than CIPT measurement due to parasitic series resistance.

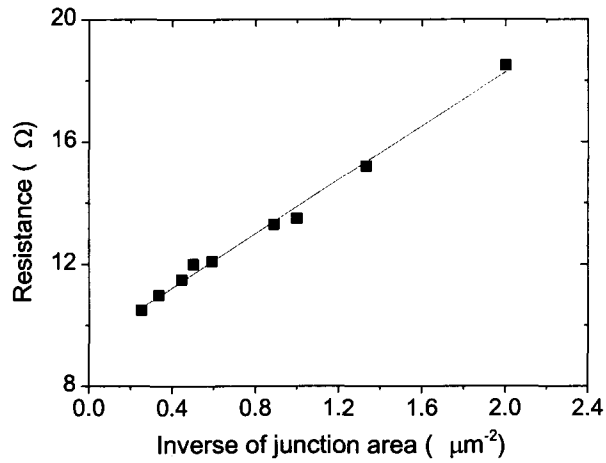


Fig. 33 Junction size dependence of resistance of MTJs. The vertical and horizontal axes show resistance of MTJs and inverse of the junction area, respectively. From the linear fitting, the parasitic series resistance (intercept) and actual RA (gradient) were evaluated to be around 10Ω and $4.4 \Omega\mu\text{m}^2$, respectively.

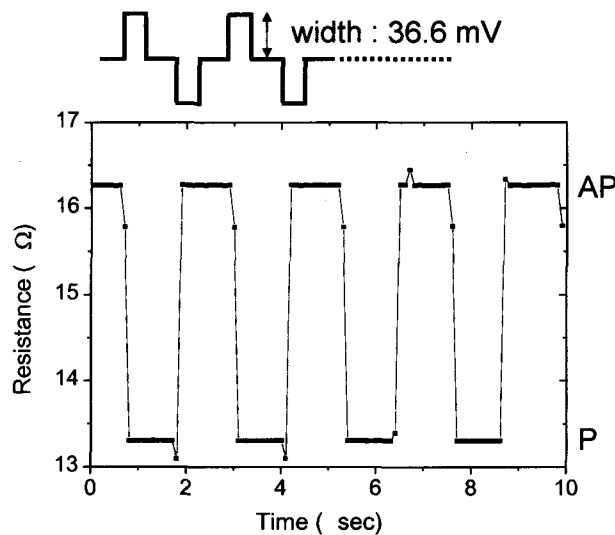


Fig. 23 Resistance change of the MTJ, induced by the successive pulse applications to the CPW. The width and amplitude of pulses are 500 ms and $\pm 36.6 \text{ mV}$, respectively. And the interval of applied pulses is also 500 ms. The resistance changes in parallel and anti-parallel states, according to pulses.

Fig. 34 shows the resistance change of the MTJ, induced by applying successive square wave pulses, 500 ms in width and ± 36.6 mV in amplitude, into the CPW. Here the external magnetic field was set at the center of the hysteresis of the MR curve, i.e., $H_{\text{ext}} = 55$ Oe. The resistance changes between 13.3Ω and 16.3Ω according to the pulse application were clearly observed. These resistances values are consistent with the resistance of parallel and anti-parallel magnetization states (R_{P} and R_{AP} , respectively).

The output power strongly depends on the bias voltage (V_{bias}) applied to the MTJ. In Fig. 35, the bias voltage dependences of the MTJ resistances for both parallel and anti-parallel configurations are shown. Following to eq. (2.26), the power gain as a function of the bias voltage applied to the MTJ is also plotted in the Fig. 35 (a). Here the input power (P_{in}) and input current (I_{in}) are calculated from the pulse voltage (36.6 mV) and the resistance of CPW ($R_{\text{CPW}} = 6.6 \Omega$), i.e. $P_{\text{in}} = (0.0366 \text{ [V]})^2 / 6.6 \text{ [\Omega]} = 0.2 \text{ [mW]}$ and $I_{\text{in}} = 0.0366 \text{ [V]} / 6.6 \text{ [\Omega]} = 5.6 \text{ [mA]}$. From the calculations, we found that the power gain of 5.6 was obtained in this device under the high V_{bias} of 0.4 V. The power gain obtained here is for the case where wire-B resistance is double of the MTJ-A resistance. For a series connection of the MTJ-A and wire-B, the short-circuit current gain, which is another important factor for this device, was estimated from experimental results and is shown in Fig. 35 (b). The current gain also increased under higher voltage application and attained a value of 0.8 at $V_{\text{bias}} = 0.4$ V.

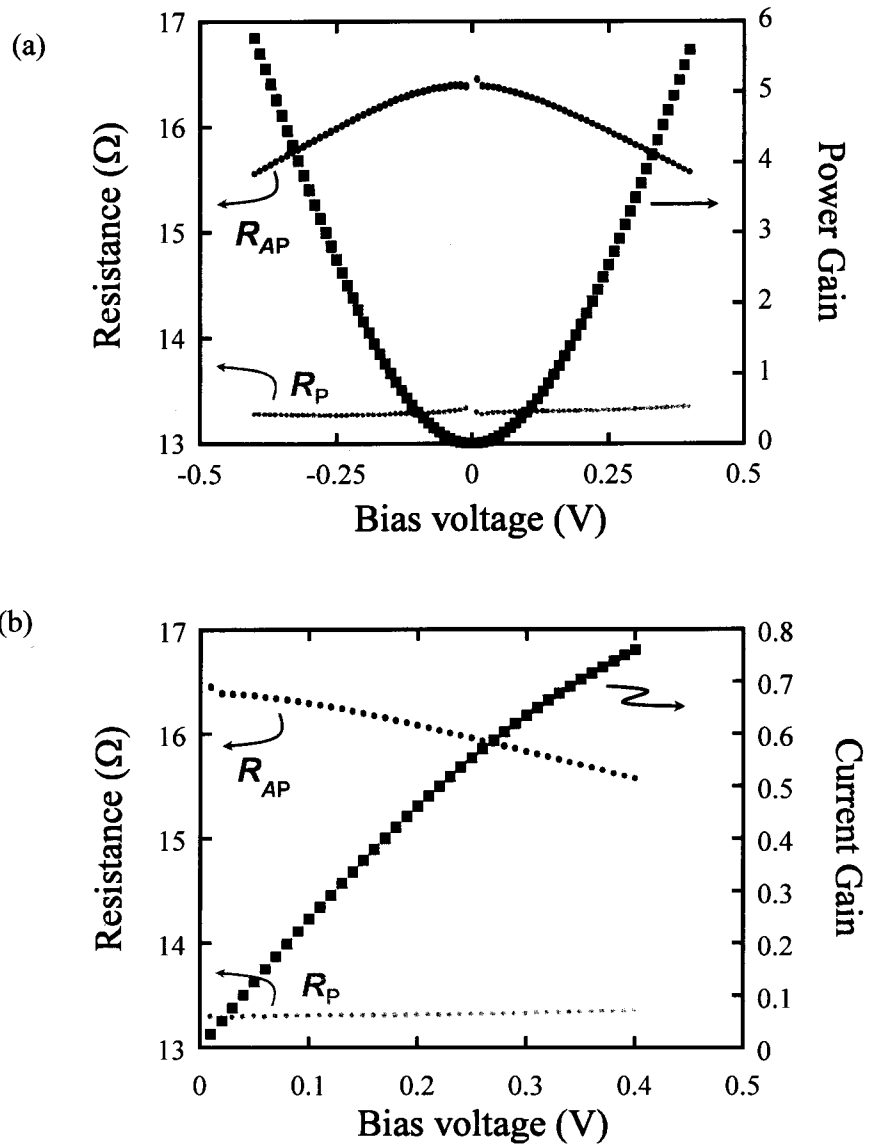


Fig. 35 Bias voltage dependence of the (a) power gain and (b) current gain. MTJ resistances in both parallel and anti-parallel configurations as a function of the bias voltage are shown in the gray curves. The power and current gain are shown as black curves. Here, the optimized load resistance is assumed to obtain higher power and current gain.

The ideal (i.e., series resistances $R_{S,T} = 0$ [Ω], $R_{S,W} = 0$ [Ω]) power gain and current gain with parasitic series resistances are shown in Fig. 36. The black dot in Fig. 36 shows the obtained power gain and current gain in the experiments. The power gain obtained in the experiment was 1% of the ideal expectation. Realistic power gains, concerning an influence of $R_{S,T} = 1$ Ω and 10 Ω are shown by light gray and gray curves in the Fig. 36(a). Including R_{series} , the gain has a peak at the optimum cell size, because the output power is mainly lost in the parasitic resistance for large MTJs with small resistance. The experimental result was quantitatively in good agreement with the theoretical expectation if we assume that the $R_{S,T} = 10$ Ω . Similar scaling is calculated for the current gain, as shown in Fig. 36 (b). We can also explain these experimental results by including the $R_{S,T}$. Although we could not obtain substantial current gain in this experiment, the calculation shows that a current gain of 10 could be obtained if we can reduce the parasitic resistance to 1 Ω . In the smaller sized device, less than 0.2 μm , it is difficult to realize the current gain in this architecture because of significant increase in H_c . To overcome this problem, use of the spin-transfer torque combined with current-field torque should be promising.

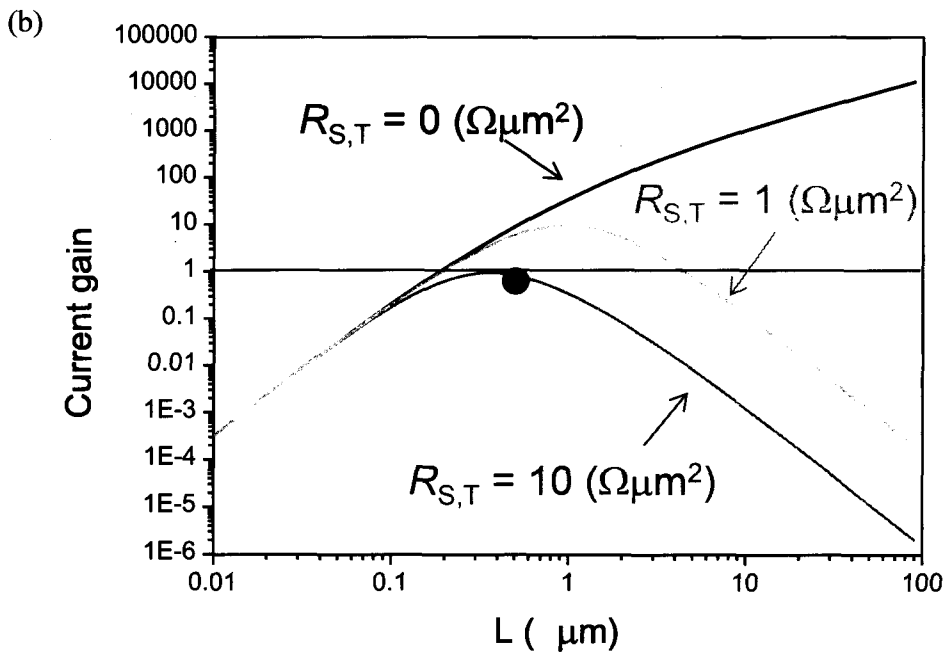
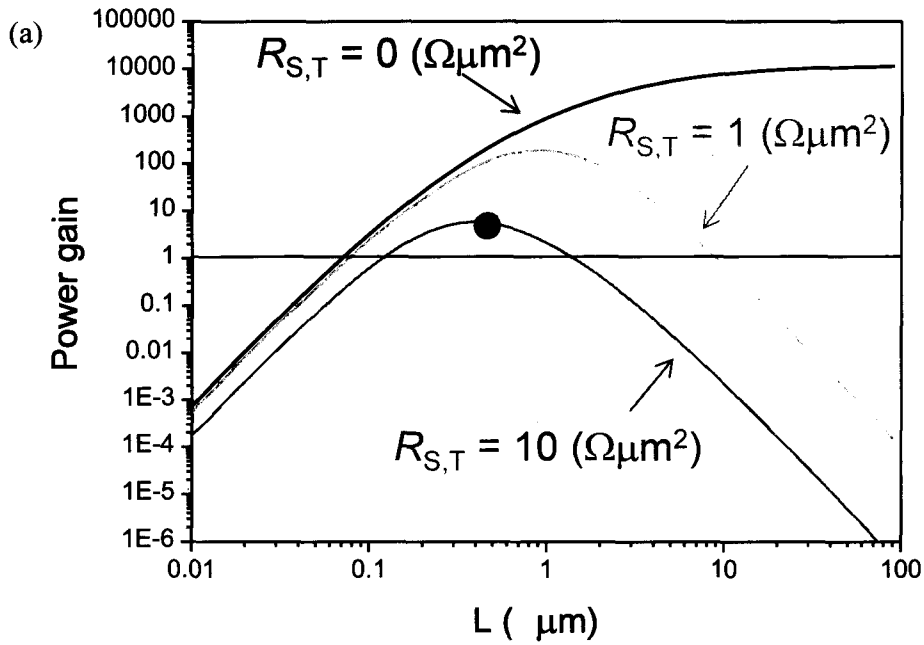


Fig. 36 The estimated (a) power gain and (b) current gain as a function of MTJ cell size L with parasitic series resistances $R_{S,T} = 0 \Omega$ (black), 1Ω (light gray), and 10Ω (gray). In the theoretical calculation, RA of $4.4 \Omega \mu\text{m}^2$ is assumed. The black dot in the figure shows the power gain or current gain obtained in the experiments, that has good agreement with the theoretical value when $R_{S,T} = 10 \Omega$.

4.2 Realization of Fan-out

In the last section, the power gain larger than 1 is demonstrated in the proposed device. However, the current gain, which is the important parameter to drive the next MTJ (MTJ-B), is less than 1. Therefore, we cannot make logic circuit using the device. In this section, the amplification properties of the current-field driven spin transistor under an assisting ac magnetic field are investigated. By reducing the effective coercivity in the free layer of the MTJ, we were able to achieve power gain of 130 and current gain of 4.9. We also could obtain a fan-out value of 5.7, i.e., the output power from the first MTJ can drive 5 additional MTJs. Simple theoretical calculations show that further improvement can be expected by optimizing the element size, the coercivity, saturation magnetization, and thickness of the free layer while maintaining relatively high thermal stability. This technique can provide a basic component of non-volatile logic devices.

MTJ structures were deposited on a thermally oxide Si substrate using magnetron sputtering (Cannon ANELVA C7100). The basic film structure is buffer layers/PtMn(15)/CoFe(2.5)/Ru(0.85)/CoFeB(3)/MgO(1.4)/CoFeB(3)/cap layers (the numbers indicate the thickness in nanometers). In particular, the thickness of MgO was estimated based on the deposition time and rate calibrated by X-ray reflectometry. The RA and MR values, which were evaluated by current-in-plane tunneling (CIPT), are $5.2 \Omega\mu\text{m}^2$ and 198%, respectively. The MTJs were patterned into junction pillars with the lateral dimensions of $0.3 \times 0.9 \mu\text{m}^2$. The width of CPW is $1 \mu\text{m}$ (the width of CPW is larger than the long axis of MTJ due to difficulty of the superposition in micro-fabrication.).

The tunneling resistance was measured by using a dc two terminal method during the application of successive pulses. The voltage of the applied pulses was monitored using an oscilloscope, which was connected in parallel with the CPW. A bias magnetic field (H_{bias}) of 40 Oe was applied to compensate the “orange peel” coupling field (Fig. 37). In addition, an assisting ac magnetic field of 2 Hz and approximately 20 Oe was applied by means of an electromagnet (schematically shown as a curve in the upper side of the Fig. 37). We can investigate the influence of the coercivity on the gain property by applying an ac magnetic field. In this study, we considered an effective field ($H_c^{\text{eff}} = 5$ Oe) to evaluate the possible maximum gain while maintaining sufficient non-volatility. It should be noted that $H_c^{\text{eff}} = 5$ Oe

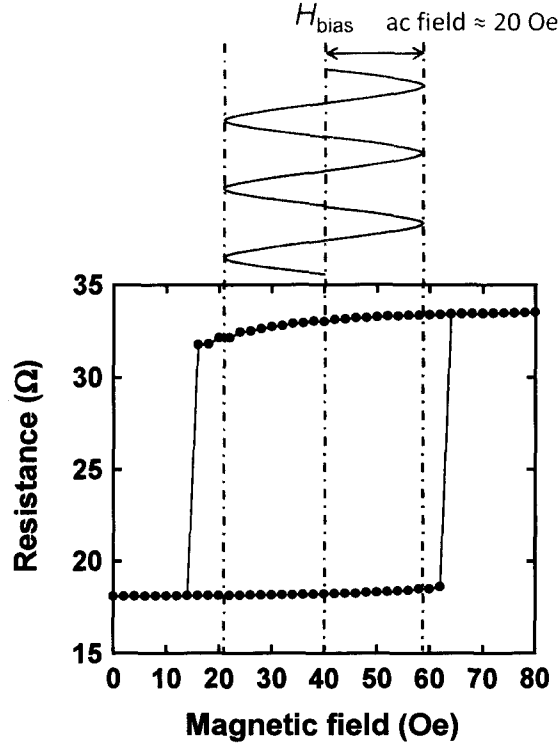


Fig. 37 A typical example of the MR curve. The lateral dimensions of MTJ is $0.3 \times 0.9 \mu\text{m}^2$. The obtained MR ratio is about 90%. The application of an assisting ac magnetic field (20 Oe) is illustrated in the upper side of the MR curve.

corresponds to $K_u = M_s H_c^{\text{eff}}/2 = 314 \text{ [J/m}^3\text{]}$, where K_u is the uniaxial anisotropy and M_s is the saturation magnetization (assumed to be 1 T for CoFeB). Therefore, even under the assisting ac field, the thermal stability factor, $\Delta = K_u \text{Vol}/k_B T$, of the free layer exceeds 60 at room temperature, thanks to the relatively large volume of the free layer, $\text{Vol} = 0.3[\mu\text{m}] \times 0.9[\mu\text{m}] \times 3[\text{nm}] = 8.1 \times 10^{-22}[\text{m}^3]$. Here, k_B and T are the Boltzmann constant and temperature.

Figure 38(a) shows examples of the applied pulses. The application of both positive and negative pulses allowed the control of the magnetization configuration in anti-parallel (AP) or parallel (P) states, as seen in Fig. 38(b). The width and maximum amplitude of each pulse are 500 ms and 10 mV, respectively. The resistance fluctuation observed in the AP state was attributed to the magnetic domain wall formation, which was induced by the external ac magnetic field. It should be noted that magnetic switching was never induced solely with the application of the ac assisting field.

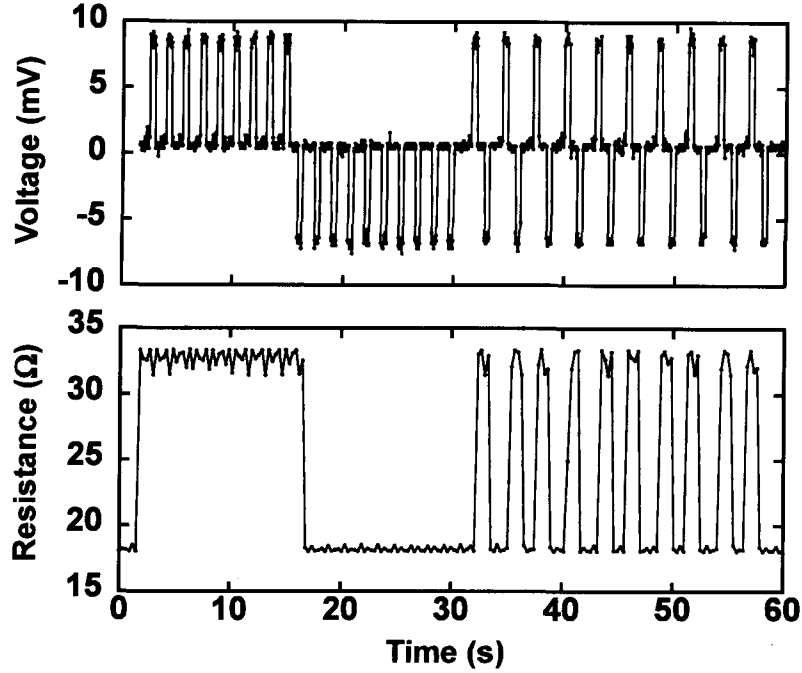


Fig. 38 (a) An example of the pulse voltages applied to the CPWs, as these are measured by the oscilloscope. (b) The resistance change in the MTJ induced by the application of voltage pulses under applying an assisting ac magnetic field. The changes in the resistance indicate the magnetization switching of the free layer in the MTJ.

Next, the power and current gain of this device are estimated, according to eq. (2.1) and eq. (2.2), in the same manner with section 4.1. At this point, the power consumed by applying the assisting ac magnetic field is neglected. Output power and current flowing through the MTJ is proportional to V^2 and V , respectively. Since the resistance of the MTJ depends strongly on the bias voltage, as seen in Fig. 39(a), both G_{power} and G_{current} are also influenced by the bias voltage. For $P_{\text{pulse}} = 0.015$ mW, the input current of 1.5 mA and CPW resistance (R_L) of 6.6Ω . We calculated G_{power} and G_{current} under the specific bias conditions. In order to estimate the maximum G_{power} , we assume that the CPW is connected in parallel with the MTJ. Under this condition, ΔP_{out} becomes maximum when $R_L = 2R_T$. Based on above estimates, we were able to obtain the maximum power gain of 130 (shown as black curve in Fig. 39).

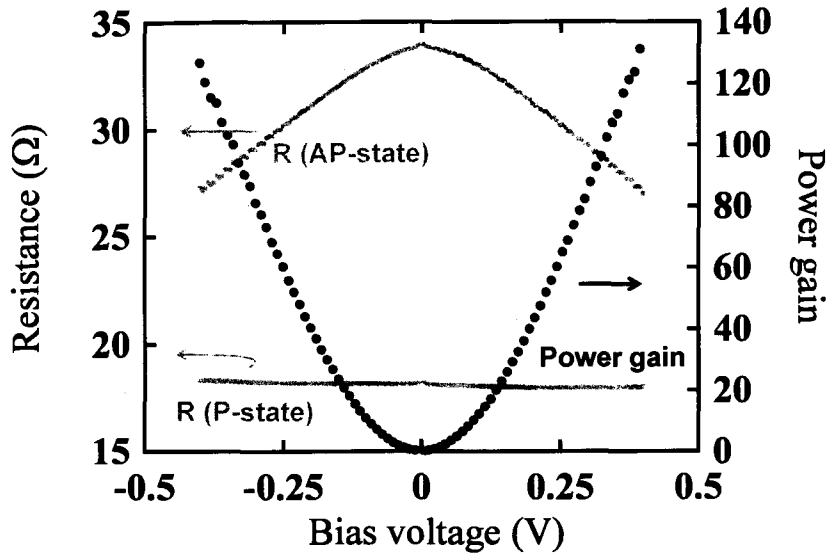


Fig. 39 Bias voltage dependence of the power gain (Black line). The MTJ resistance for both P and AP states as a function of the bias voltage is also shown as gray-colored curves. The obtained power gain becomes 23 times larger compared to Fig. 35 due to the reduction of the input power.

In contrast, the G_{current} takes its maximum value when the MTJ-A and wire-Bs are connected in series under the ideal condition that $R_L = 0$. The current gain of 4.9 (black curve in Fig. 40) is obtained at a bias voltage of 0.4 V. This relatively large enhancement could be realized thanks to the reduction in the effective coercivity of the free layer and the large MR ratio.

Of particular interest was the fan-out value, defined as the number of MTJs that can be driven by the output current. A fan-out value larger than 2 is required to use this device for logic calculations. Specifically, the fan-out value of the device is strongly related to the current gain because the device is driven by a current. In order to drive the next cell, $\Delta I_{\text{out}} > 2I_{\text{in}}$ is required for controlling the P and AP states of the additional MTJs (MTJ-B), which are driven by the output of the first MTJ. For the calculation of the fan-out value, we took into account the real load resistance (equal to the coplanar waveguide), assuming the circuit that is shown in the inset of Fig. 40. The gray color curve in Fig. 40 demonstrates the bias voltage dependence of the fan-out value. The curve was obtained by the substitution of

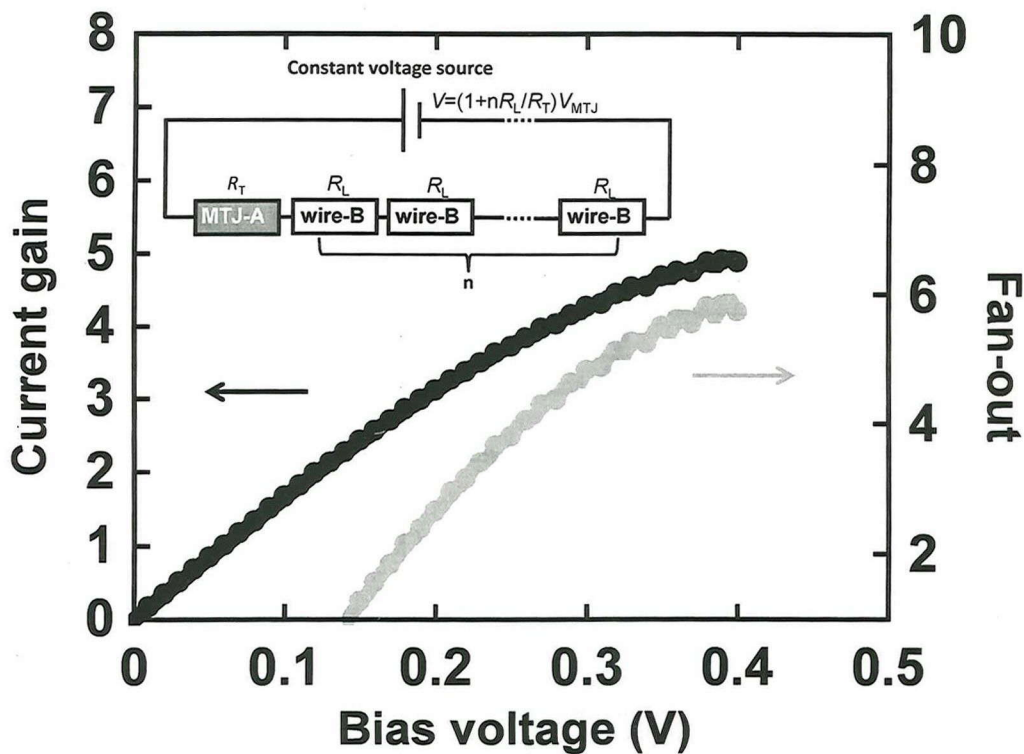


Fig. 40 Bias voltage dependence of the current gain (black line) and fan-out (gray line). Inset figure shows a schematic diagram of the electrical circuits. Current gain of 4.9 and fan-out of 5.7 are demonstrated at bias voltage of 0.4 (V)

obtained current gain to eq. (2.40), which is introduced later. A fan-out value of 5.7 under is obtained at a bias voltage of 0.4 V, indicating that 5 cascaded MTJs can be driven by the output of the first MTJ. This implies that the current-field driven spin transistor has the capability to work as a basic element of a nonvolatile logic device if we can reduce the coercivity of the free layer while maintaining relatively high thermal stability.

For this study, we applied a dc pulse with a long time duration of 500 ms. When the pulse duration time is reduced to nanosecond order, the current required for switching becomes larger, following the thermal assisted model. Therefore, the fan-out value may be reduced under a gigahertz operation.

In the last part of this session, I show the scaling of the fan-out value of this device. When the size of an MTJ is large enough, the distance between the wire and free layer of the MTJ can be considered negligible. Consequently, the current required for switching (I_{in}) can be written as $I_{in} = 2wH_c^{eff}$, where w is the width of

the wire. To estimate the fan-out value, MTJ-A and n-wire-Bs are assumed to be connected in series, as shown in the inset of Fig. 40. In the case of application of assisting ac magnetic field, eq. (2.41) can be rewritten as eq. (4.1) using the effective coercive field (H_c^{eff}),

$$\text{Fan-out} = \frac{R_T}{R_L} \left(\frac{V_{\text{MTJ}} \times \text{MR}^*}{2 \times 2wH_c^{\text{eff}} \times R_T} - 1 \right) \quad \dots (4.1)$$

In the calculation of fan-out value shown in Fig. 41, I assumed $w = 3L$ (L is the size of MTJ and factor 3 indicates the aspect ratio of the junction pillars), $R_T = \text{RA} / 3L^2$, R_L is the wire resistance, defined as $R_L = \rho l / wt$, ρ is the resistivity, l is the length and t is the thickness of the wire, respectively (details of the calculation are included in the Appendix). Fig. 41 shows the expected fan-out as a function of L and the effective coercivity (H_c^{eff}). For this calculation, the following values for the wire parameters were used: $\rho = 2 \times 10^{-7} [\Omega \cdot \text{m}]$, $l = 10L$ and $t = 100 \text{ nm}$. According to the experimental results, the MR ratio is 100% ($\text{MR}^* = 2/3$), the distance between wire and free layer of MTJ is 140 nm (thickness of the top electrode and the SiO_2 insulating layer) and the RA value is $5 \Omega \mu\text{m}^2$. Furthermore, we took into account the influence of the series resistance (R_s), which results from parasitic resistance, such as each electrode's resistance. Subsequently, R_T in (4.1) should be substituted by $R_T + R_s$. It also affects the MR^* .

The dot in the Fig. 41 represents the experimental result. The R_s of our device was estimated to be approximately 7Ω . The obtained result is in good agreement with the theoretical estimate. By taking into account the series resistance, the fan-out value becomes less than 1 when L is comparatively large, because the series resistance causes a reduction in the MR ratio. The area above the lines in Fig. 41 represents a region in which $\Delta > 60$. Since the product $M_s t$ plays affects Δ , two examples of border lines for $M_s t = 3$ (this experiment) and $30 [\text{T} \cdot \text{nm}]$ are illustrated (t is the thickness of the free layer). Further enhancement of the fan-out value can be realized by increasing the saturation magnetization and/or the thickness of the free layer by reducing H_c^{eff} . The fan-out value becomes smaller in the deep-submicron range.

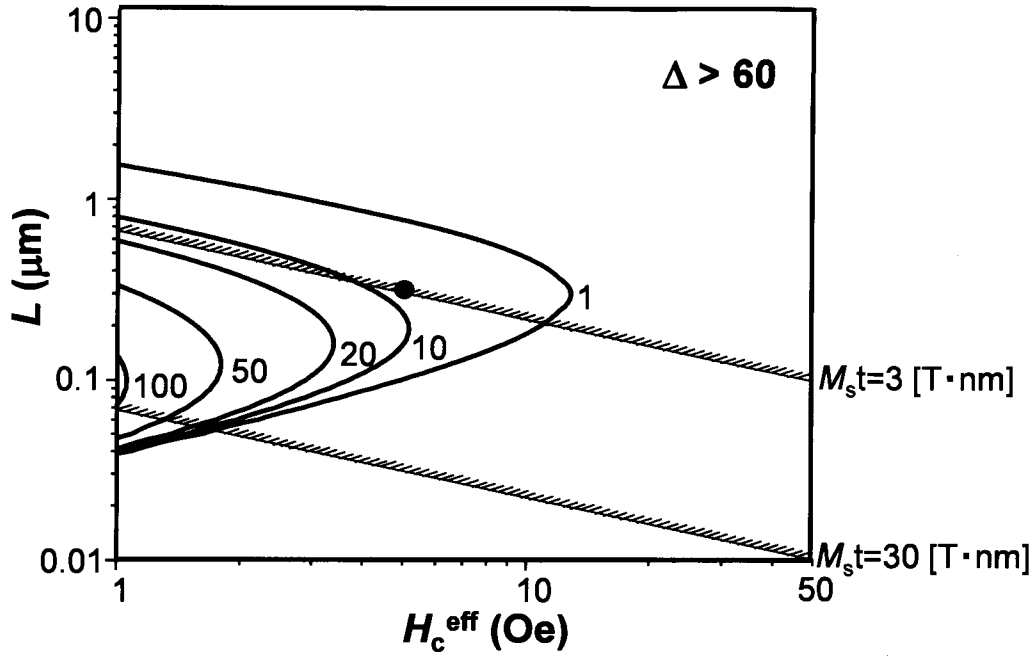


Fig. 41 The estimated fan-out value as a function of the MTJ cell size L and the effective coercivity. For the calculations, $MR = 100\%$, $RA = 5 \Omega\mu\text{m}^2$, and $V_{\text{MTJ}} = 0.4 \text{ V}$ are assumed and finally, R_{series} of 7Ω for the actual device. The lateral dimension of the MTJ cell is $L \times 3L$. The width of the CPW and the thickness of the SiO_2 insulating layer are $3L$ and 140 nm , respectively. The area above the lines corresponds to a region in which the thermal stability factor is higher than 60 when $M_s t = 3$ and $30 \text{ [T}\cdot\text{nm]}$. The dot represents the experimental result.

To summarize section 4.1 and 4.2, the characteristics of current-field driven spin transistor is investigated. The power gain is firstly obtained in a spin transistor at RT. Fig. 42 shows the development of gain in any spin transistor at RT. Except for the report of current gain (performed at 2.6 K), this study shows the amplification effect in spin transistor. The fan-out value, which has not been discussed in spin transistor, of about was successfully obtained. From these results, the current-field driven spin transistor satisfies Boolean operations.

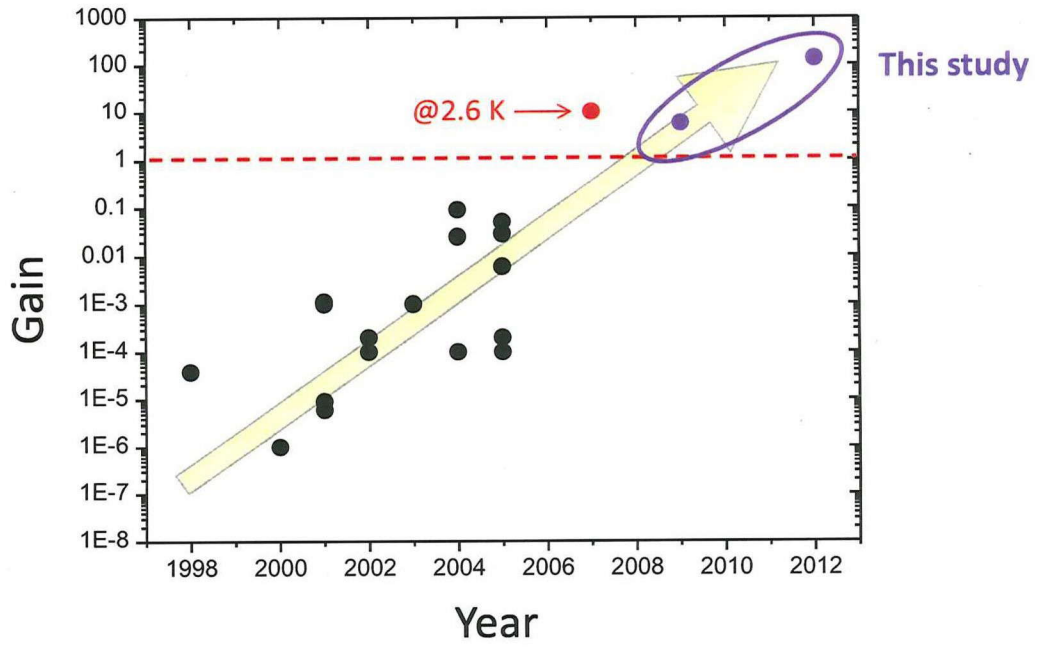


Fig. 42 The development of gain in any spin transistors at RT. Except for the report of current gain at low temperature (2.6 [K]), this study is firstly obtained gain > 1 in a spin transistor.

4.3 RF amplification

In the section 4.1 and 4.2, the amplification properties and fan-out of the current-field driven spin transistor are shown. In this section, the radio-frequency (RF) voltage amplification property of a tunnel magnetoresistance device driven by an RF external-magnetic-field-induced ferromagnetic resonance is studied in the same type of devices. The input RF voltage applied to the waveguide can excite the resonant dynamics in the free layer magnetization, leading to the generation of an output RF voltage under a DC bias current. The dependences of the RF voltage gain on the static external magnetic field strength and angle were systematically investigated. The design principles for the enhancement of the gain factor are also discussed.

Thus far, several RF amplification properties of an MTJ structure have been proposed and demonstrated experimentally. The study by Slonczewski^[63] was the first to propose the above mentioned properties. The other concepts of RF amplification have been proposed using negative differential resistance^[64], vortex-core resonance^{[65],[66]}, and spin-torque-induced ferromagnetic resonance in an MTJ^[67]. These devices for RF amplification were combined with the spin-transfer torque effect.

A schematic structure of the proposed device with the measurement circuit is shown in Fig. 31. When a coplanar waveguide (CPW) is combined with an MTJ, an RF magnetic field is generated around the CPW under an application of RF current to the CPW. Further, ferromagnetic resonance (FMR) is induced when the frequency of the RF magnetic field is tuned to the resonant frequency of magnetization of the free layer in the MTJ. Generally, magnetization precession can be excited efficiently under the resonance condition, leading to the generation of a large RF output voltage from the MTJ under a large DC bias current. If the output voltage exceeds the input voltage, the proposed device can be used for the amplification of RFs.

MTJ films with a structure of buffer layers/PtMn/CoFe/Ru/CoFeB(3)/MgO (1.1)/CoFeB(3)/Ru(1.5)/NiFe(2)/capping layers (nm in thickness) were deposited on Si/SiO₂ substrates using a magnetron sputtering method (Canon ANELVA C7100). From the current-in-plane tunneling (CIPT) measurements, the resistance-area product and the magneto-resistance ratio were evaluated to be 3.8 $\Omega\mu\text{m}^2$ and 110%, respectively. The multilayer film was patterned into junctions ($0.3 \times 0.6 \mu\text{m}^2$) with

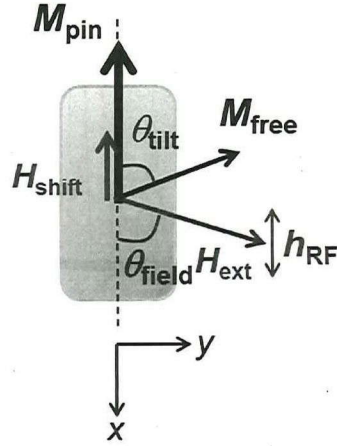


Fig. 43 Schematic image of the configuration of magnetization and magnetic fields. M_{free} and M_{pin} denote the magnetization of the free and pinned layer; θ_{tilt} and θ_{field} indicate the relative angle and the angle of the external magnetic field; and h_{RF} , H_{ext} , and H_{shift} indicate the RF magnetic field, the external magnetic field, and shifted field, respectively.

ctrically isolated coplanar waveguide (the width of CPW is $0.8 \mu\text{m}$). The RF power, which generates the RF magnetic field, was applied at port-1 (V_{in}) of the vector network analyzer (VNA). Further, a bias current was applied to the MTJ through a DC port of the bias Tee. The output signal from the MTJ (V_{out}) was detected by port-2 of the VNA. The RF amplification property was evaluated by monitoring the S_{21} ($= V_{\text{out}}/V_{\text{in}}$) parameter. The magnetization configurations of the pinned and free layers and the magnetic field are shown in Fig. 43. The x -axis (direction perpendicular to the CPW) is defined to be parallel to the easy axis of the free layer. The external magnetic field, H_{ext} , is applied along the direction with angle θ_{field} from the x -axis. The S_{21} parameter was measured under various H_{ext} and θ_{field} conditions. The input RF power and the DC bias current were fixed at $20 \mu\text{W}$ and -8 mA in all the measurements. Here, the positive current is defined as one in which the electrons flow from the free layer to the pinned layer.

In order to extract the FMR signal clearly, the background signal, which originates from the transmission property of the CPW, was subtracted from the raw S_{21} data. The background signal was obtained under the sufficiently large $H_{\text{ext}} = 1 \text{ kOe}$ applied along the direction of the x -axis, because the FMR could not be induced in this configuration. In this study, ΔS_{21} indicates the measured S_{21} parameter without the background.

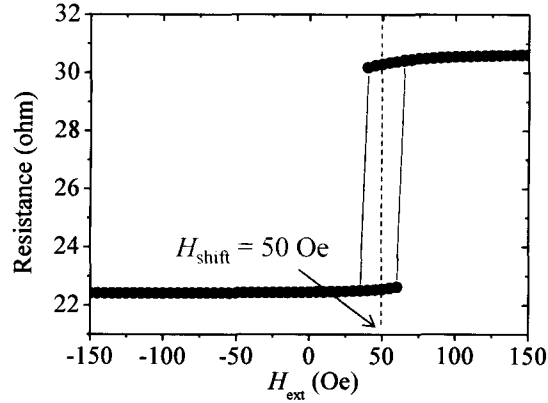


Fig. 44 Typical MR curve ($\theta_{\text{field}} = 0^\circ$). The free layer of the MTJ consists of CoFeB (2 nm) / Ru / NiFe (2 nm) ferromagnetic coupled layer. The junction size is $0.3 \times 0.6 \mu\text{m}^2$. The obtained MR ratio is about 38%. From this curve, H_{shift} is defined as 50 Oe.

Fig. 447 shows the typical MR curve when θ_{field} is 0° . The obtained MR ratio became three times smaller than that obtained by the CIPT measurement, owing to the influence of the parasitic series resistance. A shift field of 50 Oe was obtained, which is caused by orange-peel coupling (a parallel state is preferred under zero magnetic field). The measured gain factor (i.e., the absolute value $[\Delta S_{21}]$, which is hereafter simply called ΔS_{21}) as a function of frequency is shown in Fig. 45 (a), where θ_{field} was fixed at 55° . Depending on the strength of the external magnetic field, the amplitude of ΔS_{21} and the resonant frequency were changed, indicating that the FMR excitation was induced by the application of the RF signal to the CPW. The value of ΔS_{21} becomes small when $H_{\text{ext}} = 50$ Oe, possibly because of the inhomogeneous precession motion attributed to multi-domain formation. The observed resonant frequency was plotted as a function of the external magnetic field with $\theta_{\text{field}} = 55^\circ$ in Fig. 38 (b). The observed shift was well reproduced by Kittel's formula (red curve in the same figure). From the fitting, the in-plane and out-of-plane anisotropy fields were evaluated to be 15 Oe and 7500 Oe, respectively. Fig. 46 (a) shows $\Delta S_{21_{\text{max}}}$ as functions of the strength and angle of H_{ext} . Here, we define $\Delta S_{21_{\text{max}}}$ as the peak height of ΔS_{21} at each angle and external magnetic field. The red area indicates the high amplification gain, which reaches the maximum value of approximately 0.07.

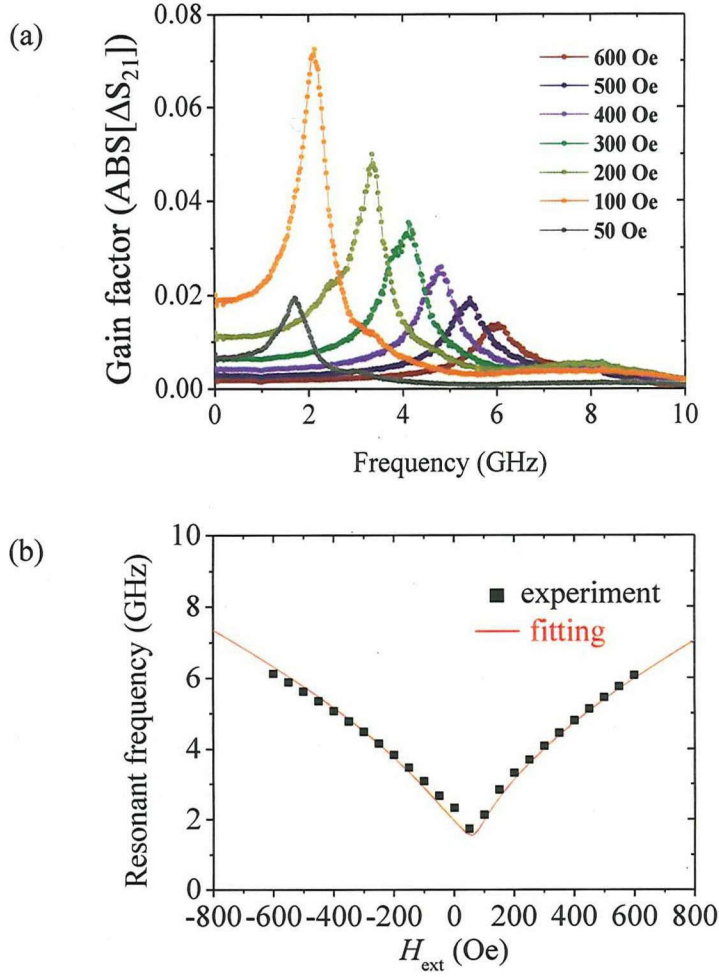


Fig. 45 (a) Gain factor (absolute value [ΔS_{21}]) as a function of frequency ($\theta_{\text{field}} = 55^\circ$). (b) Resonant frequency as a function of the external magnetic field ($\theta_{\text{field}} = 55^\circ$). The black dots and red curve show the experimental results and the fitting curve, respectively. From the fitting, the in-plane and out-of-plane anisotropy fields were evaluated to be 15 Oe and 7500 Oe, respectively.

The output voltage from the MTJ ($V_{\text{out}}(\omega)$) for small precession angles is described by eq. (4.2) [42].

$$V_{\text{out}}(\omega) = \eta'(\omega) \frac{R_{\text{AP}} - R_{\text{P}}}{4\sqrt{2}} i_0(\theta_{\text{prec}}) \sin(\theta_{\text{tilt}}) \quad \dots (4.2)$$

where $\eta'(\omega)$ is the efficiency of the RF circuit; R_{P} and R_{AP} are the resistances in parallel and anti-parallel states, respectively; i_0 is the bias current; θ_{prec} is the precession angle; and θ_{tilt} denotes the relative angle between the pinned and free layer magnetization. When $\theta_{\text{field}} = 55^\circ$ and $H_{\text{ext}} = 100$ Oe, a relative angle of $\theta_{\text{tilt}} = 83^\circ$

was obtained by resistance monitoring. The largest RF gain factor was obtained at this field and angle. This behavior is consistent with eq. (4.2). Furthermore, the resonant frequency decreases with a decrease in the external magnetic field, which in turn results in an increase in the precession angle^[68]. From the above discussion, it can be concluded that it is important to reduce the resonant frequency and obtain a relative angle of 90° to obtain a large output.

Here, we compare the experimental results with the simulation results. Using the parameters obtained from our experiments and from Kittel's fitting, we simulated the RF gain by using a macro-spin model based on the Landau-Lifshitz-Gilbert eq. Fig. 46 (b) shows the simulated result as functions of H_{ext} and θ_{field} . We assume that the damping factor $\alpha = 0.01$ and temperature $T = 300$ K. Here, the influence of the thermal effect is treated as a random magnetic field^{[69],[70]}. The experimental results were well reproduced qualitatively by this simple simulation. However, in the simulation, the maximum gain was obtained for both a small magnetic field and a small tilt angle at around $H_{\text{ext}} = 50$ Oe and $\theta_{\text{field}} = 15^\circ$. At this field and angle, the shift field and in-plane magnetic anisotropy are cancelled simultaneously by the external magnetic field. Subsequently, the resonant frequency becomes very low and the RF gain increases. However, this condition is difficult to achieve in the experiment, because a multi-domain structure is formed in the low magnetic field range. Further, the simulated gain is approximately 5 times greater than that obtained by the experimental result. In the experiment, the linewidth of the FMR peak is broadened because of non-uniform precession attributed to a relatively large sample size. This leads to a small Q-value (~ 2) in the experiment, and consequently, the gain factor becomes smaller than expected.

The RF gain does not exceed 1 even in the simulation. One possible approach to realize high RF amplification is to introduce perpendicular magnetic anisotropy. When the out-of-plane anisotropy is cancelled by the external magnetic field, a high Q-value of 50 can be obtained^[71]. This value is 25 times greater than that obtained by our results. Thus, the RF gain factor can exceed 1 if we apply their condition (i.e., using Fe-rich CoFeB free layer for perpendicular magnetic anisotropy^{[72],[73]} and applying external magnetic field to cancel demagnetization field) to our experiment.

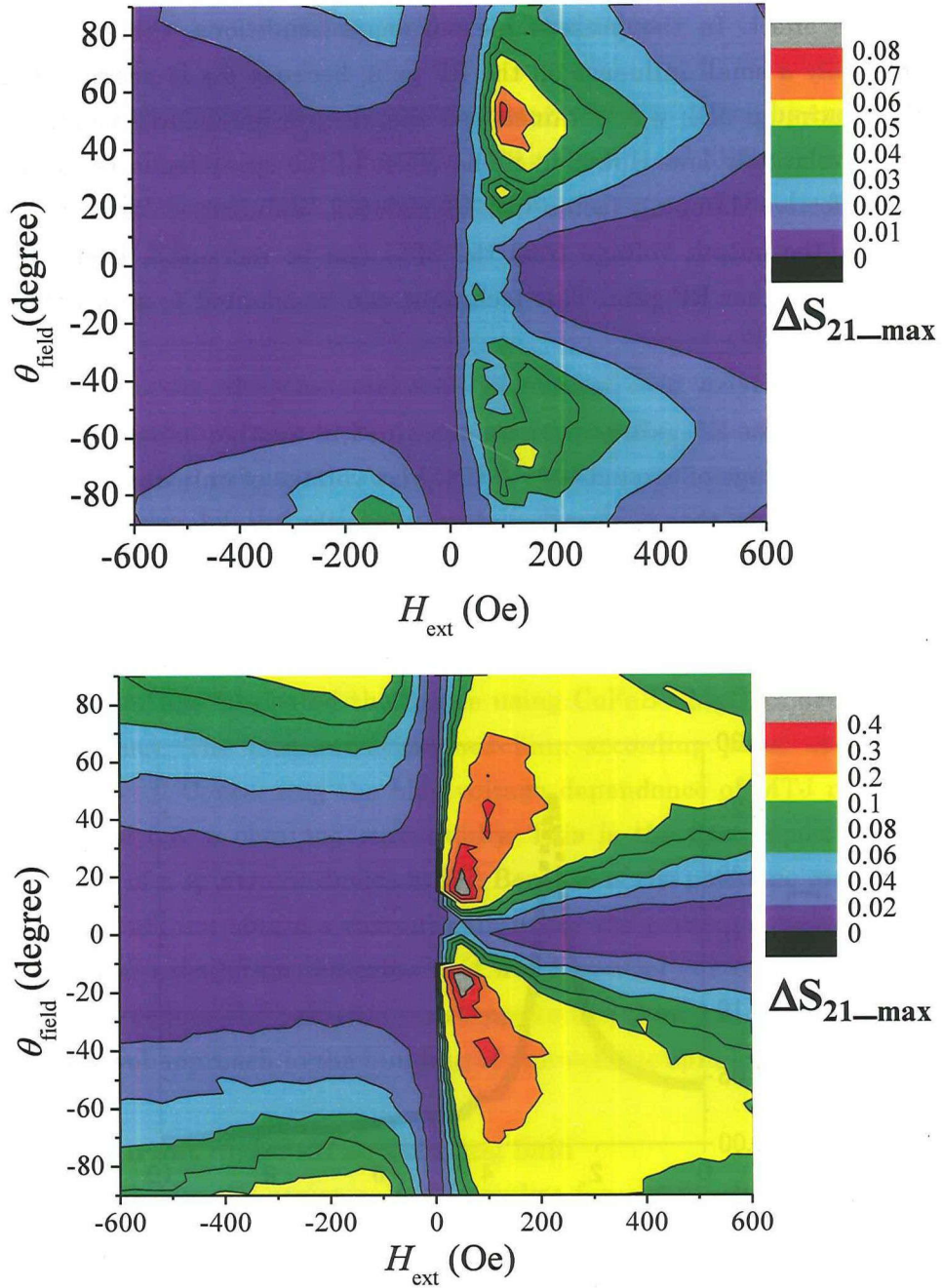


Fig. 46 S_{21_max} as functions of θ_{field} and H_{ext} . (a) Experimental result and (b) simulated result by macro-spin simulation. From (a), the maximum obtained RF gain is about 0.07 when $\theta_{field} = 55^\circ$ and $H_{ext} = 100$ Oe. From (b), the maximum gain is obtained when $\theta_{field} = 15^\circ$ and $H_{ext} = 50$ Oe, where in-plane and out-of-plane anisotropy can be cancelled by external magnetic field.

Another possible approach to enhance the RF gain factor is to utilize the spin transfer effect. In the present measurement conditions, the spin transfer torque has only a small influence on the RF gain, because θ_{tilt} is nearly 90 degree when the maximum ΔS_{21} was obtained and the electric breakdown voltage of the sample was relatively low. However, if the effect of the spin torque is sufficiently large, the effective damping factor will be reduced, inducing a large precession angle; hence, the output voltage from the MTJ can be increased, leading to the realization of a higher RF gain. This technique can be adapted to a magnetic field feedback oscillator^[74].

Recently, the RF gain of 0.27 was obtained in another sample by applying larger DC bias voltage of around 0.4 (V) (DC bias voltage of only about 0.2 (V) was applied to the sample, that is discussed above, since the breakdown voltage of MgO is relatively low in the sample). An example of result are shown in Fig. 47. RF gain of 0.27 is the maximum value in the all reports up to now.

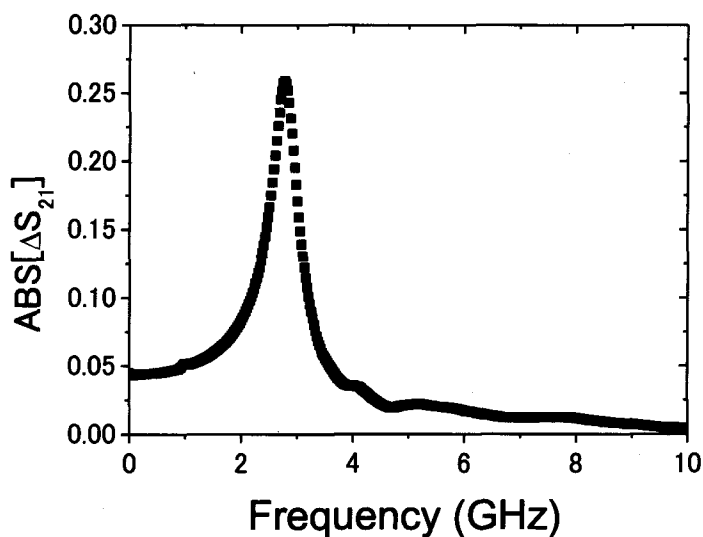


Fig. 47 RF gain factor (ABS[ΔS_{21}]) as a function of frequency. The RF gain achieved to 0.27 under an application of bias voltage of 0.4 (V).

Chapter 5 Conclusion

The current-field driven spin transistor, which is driven by current-induced magnetic field, is proposed in this study. Using MgO-based high performance MTJs, the device is fabricated. And the amplification properties of the device are mainly investigated at RT.

Scaling

To compare the characteristics of current-field driven and spin torque driven spin transistors, new types of spin transistors are proposed. Following to the scaling models, the power gain and the fan-out value are verified as a function of MTJ feature size by theoretical approach. From the scaling of the fan-out, I conclude that current-field driven spin transistor is suitable for Boolean operation.

Power amplification

The author fabricated the device using CoFeB / MgO / CoFeB MTJs with low RA product. The magnetization switching according pulse applications are clearly observed. Concerning the bias voltage dependence of MTJ resistance, the power gain of 5.6 is obtained successfully. This is the first report of the power amplification of a spintronic device at RT. Because of the parasitic resistance of the system, we could not obtain a current gain under the present conditions. However, the theoretical calculation indicates that a substantial current gain of 10 can be realized if we reduce the parasitic resistance to less than 1 Ω . Our suggestion may open up a novel approach to the building of non-volatile spin logic devices.

Gain and Fan-out under an ac assisting field

To enhance the power gain and realize fan-out function in the device, the amplification properties of a current-field driven spin transistor under an ac assisting magnetic field is investigated. A power and current gain as high as $G_{\text{power}} = 130$ and $G_{\text{current}} = 4.9$ were successfully demonstrated, those values are much higher than that of without ac magnetic field due to the reduction in the input power and the input current. These improvements made it possible to realize a fan-out value of 5.7. A reduction in the parasitic resistance and high MR ratios were necessary to obtain the highest fan-out value. Through the device scaling, further increase in the fan-out value—as high as 10—can be expected by optimizing the element size, free

layer thickness and saturation magnetization.

Although the ac magnetic field is not indispensable for the basic operation, it may be useful to enhance the element selectivity while maintaining high thermal stability. A simple wave guide structure can be easily implemented in the proposed device.

As already discussed in the development process of current-field driven MRAM devices, it is difficult to realize the high thermal stability and small switching current at the same time for the case of in-plane magnetized film. One promising solution is to use a perpendicularly magnetized film with the spin transfer effect. Additionally, microwave assisted magnetization reversal^{[75]-[77]} and voltage-induced magnetization switching should be helpful in improving the performance of the proposed spin transistor.

RF amplification

The amplification property of MTJs afforded by the magnetic-field-induced FMR was proposed and demonstrated. A maximum voltage gain of 0.07 was achieved under the optimized external magnetic field condition. In addition, the static external magnetic field strength and angle dependences of the voltage gain were systematically investigated and reproduced qualitatively by a simple macro-spin model simulation. The improvement of the uniform precession in the element, as well as the introduction of perpendicular magnetic anisotropy or the spin transfer effect, were shown to be effective in achieving RF voltage gains greater than 1. Further, the RF gain of 0.27 was obtained in another sample. The increase in RF gain is because large DC bias voltage can be applied to the sample due to high withstands voltage. The obtained value is the highest in the previously reported values.

From these results, logic circuits can be formed using only MTJs. Fig. 48 shows the schematic diagram of the concept device. When RF signal is caught by antennas, the signal can be detected by spin torque diode effect. After detection, the signal is amplified and calculated by current-field driven spin transistors. On the other hand, non-volatile logic circuit, consisting of current-field driven spin transistors, calculates. The information is applied into spin torque oscillator. After that, RF signal can be amplified by spin transistors and emitted to external through an antenna. This device can be used in mobile devices due to low power consumption in non-volatile logic circuits.

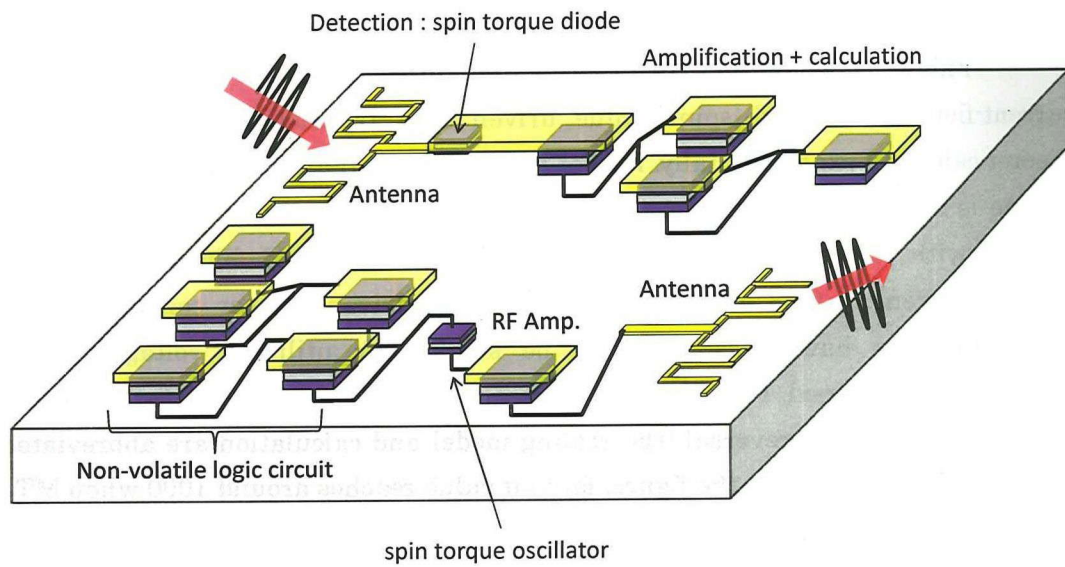


Fig. 48 schematic diagram of the concept device. Current-field driven spin transistors can be used as an amplifiers and non-volatile logic circuits.

Future prospective

Finally, I would like to describe the future prospective. In this study, current-field driven and spin torque driven spin transistors are investigated theoretically and experimentally. Recent years, voltage induce magnetic anisotropy change is rapidly developing as the next way to control magnetization direction. Similar with semiconductor transistors, which is changed bipolar transistor (current driven) to field effect transistor (voltage driven), power consumption in spin transistors have possibilities to be smaller by utilizing voltage control magnetization reversal. Fig. 49 shows the scaling of fan-out value, utilizing voltage control magnetization reversal (the scaling model and calculation are abbreviated in this study). As shown in the figure, fan-out value reaches around 1000 when MTJ size is small. By comparison to current-field driven and spin torque driven types, voltage driven spin transistor has large potential to become next generation spin transistor. I would like to finish this thesis with expectation of new type of spin transistors.

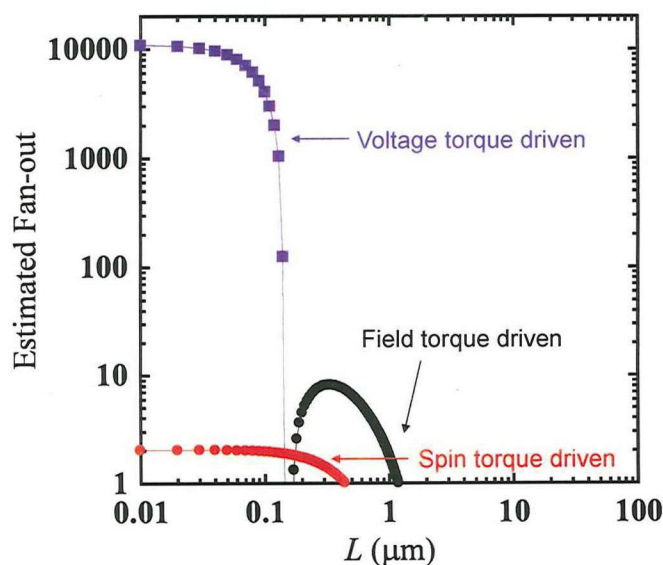


Fig. 49 The scaling of fan-out value. Blue curve shows the fan-out value in the voltage driven spin transistor. Black and red curves shows fan-out values of field driven and spin torque driven spin transistors, which are same as Fig. 24.

Acknowledgement

Here, I would like to express my sincere gratitude to many persons for their help to my study of Ph. D. Firstly of all, I would like show my deep appreciation to my Ph. D. advisor Professor Yoshishige Suzuki (Professor, Osaka University, Japan). He instructed me both conducting experiments and understudying physics. I learned a lot of things from him, such as how to use experimental equipment correctly, how to measure good data and how to analyze data. Besides, he gave me an opportunity to study abroad, which provided me great improvement as a researcher. I am really proud that I learned 6 years in Prof. Suzuki's laboratory.

Also I would like to express my great gratitude to Dr. Takayuki Nozaki (Assistant professor, Osaka University, now a member of AIST) and Mr. Shinji Miwa (Assistant professor, Osaka University) for their kind help. They always gave me good advices and discuss empathically. I became able to get Ph. D thank to their help.

I would also like to appreciate Dr. Shinji Yuasa (leader of Spintronics Research Group, AIST), Dr. Akio Fukushima, Dr. Hitoshi Kubota, Mr. Hiroki Maehara and other members in AIST. They provided high-quality CoFeB / MgO / CoFeB MTJ films for this study. Besides, they taught me the film fabrication and micro-fabrication process. They also discussed with me about the properties of MTJ films to obtain higher amplification properties in my device.

Concerning RF amplification experiments, I would like to express my appreciation for Dr. Ashwin A. Tulapurkar (Associate professor in Indian Institute of Technology : IIT) and Mr. Dinesh K Dixit (IIT) for their cooperation. Especially, I learned a lot of thing from conducting experiments with Prof. Ashwin. He gave me fruitful advices about measurements.

Next, I would like to express my appreciation for Professor Theo Rasing, Dr. Andrei Kirilyuk, Dr. Alexey Kimel, Mr. Ali Reza Khorsand and member of Radboud University Nijmegen, Institute for Molecules and Materials. They instructed and helped me with optical pump and probe measurement. I enjoyed studying and staying in Nijmegen, this is by kindness of them.

I would also like to appreciate Prof. Eiichi Tamura (Professor, Osaka University, Japan) for his kind help, especially in theory. He always answers my questions kindly and adequately even when my questions are quite trivial. Further, my life in laboratory was made joyful and fruitful thanks to his activities.

Finally, I would like to express my thanks to Professor Norikazu Mizuochi, Professor Teruya Shinjo, Professor Masashi Shiraishi, Dr. Frederic Bonell, Ms. Yumi Oda, Ms. Rie Hasegawa, Mr. Tadahiro Sugimura and Ms. Kazuyo Nakajima (staffs of Graduate School of Engineering Science, Osaka University) for their advices and supports. I would also like to thank all other members in Professor Suzuki's group.

References

- [1] W. Thomson, Proc. Roy. Soc. (London) **8**, 546 (1857)
- [2] C. Kittel, "Introduction to the solid state physics", 7th edition, p232, John Wiley & Sons, Inc.
- [3] T. R. Mcguire and R. I. Potter, IEEE Trans. Magn. MAG-1, 1018 (1975)
- [4] G. Binasch, P. Grunberg, F. Saurenbach and W. Zinn, *Phys. Rev. B*, **39**, 4828 (1989).
- [5] M. N. Baibitch, J. M. Broto, A. Fert, F. Nguycn Van Dau and F. Petroff, *Phys. Rev. Lett.*, **61**, 2472 (1988).
- [6] M. Julliere, *Phys. Lett.*, **54A**, 225 (1975).
- [7] T. Miyazaki and N. Tezuka, *J. Magn. Magn. Mater.*, **139**, L231 (1995).
- [8] J. S. Moodera, Lisa R. Kinder, Terrilyn M. Wong and R. Meservey, *Phys. Rev. Lett.*, **74**, 3273 (1995).
- [9] W. H. Butler, X-G. Zhang, T. C. Schulthess and J. M. MacLaren, *Phys. Rev. B*, **63**, 054416 (2001).
- [10] J. Mathon and A. Umerski, *Phys. Rev. B*, **63**, 220403 (2001).
- [11] S. Yuasa, A. Fukushima, T. Nagahama, K. Ando and Y. Suzuki, *Jpn. J. Appl. Phys.*, **43**, L588 (2004).
- [12] S. Yuasa, A. Fukushima, T. Nagahama, Y. Suzuki and K. Ando, *Nature Mater.*, **3**, 868 (2004).
- [13] S. S. Parkin, C. Kaiser, A. Panchula, P. M. Rice, B. Hughes, M. Samant and S-H. Yang, *Nature Mater.*, **3**, 862 (2004).
- [14] D. D. Djayaprawira, K. Tsunekawa, M. Nagai, H. Maehara, S. Yamagata, N. Watanabe, S. Yuasa, Y. Suzuki and K. Ando, *Appl. Phys. Lett.*, **86**, 092502 (2005).
- [15] S. Ikeda, J. Hayakawa, Y. Ashizawa, Y. M. Lee, K. Miura, H. Hasegawa, M. Tsunoda, F. Matsukura and H. Ohno, *Appl. Phys. Lett.*, **93**, 082508 (2008).
- [16] J. C. Slonczewski, *J. Magn. Magn. Mater.*, **159**, L1 (1996).
- [17] L. Berger, *Phys. Rev. B*, **54**, 9353 (1996).
- [18] J. C. Slonczewski, *Phys. Rev. B*, **71**, 024411 (2005).
- [19] T. L. Gilbert, *Phys. Rev.*, **100**, 1243 (1955).
- [20] L. Landau and E. Lifshits, *Phys. Zeitsch. Der Sow.* **8**, 153 (1935).
- [21] E. B. Myers, D. C. Ralph, J. A. Katine, R. N. Louie and R. A. Buhrman, *Science*, **285**, 867 (1999).
- [22] J. A. Katine, F. J. Albert, R. A. Buhrman, E. B. Myers and D. C. Ralph, *Phys. Rev. Lett.*, **84**, 3149 (2000).

- [23] F. J. Albert, J. A. Katine, R. A. Buhrman and D. C. Ralph, *Appl. Phys. Lett.*, **77**, 3809 (2000).
- [24] J. Grollier, V. Cros, A. Hamzic, J. M. George, H. Jaffres, A. Fert, G. Faini, H. Ravera, J. Ben Youssef and H. Legall, *Appl. Phys. Lett.*, **78**, 3663 (2001).
- [25] Y. Huai, F. Albert, P. Nguyen, M. Pakala and T. Valet, *Appl. Phys. Lett.*, **84**, 3118 (2004).
- [26] H. Kubota, A. Fukushima, Y. Ootani, S. Yuasa, K. Ando, H. Maehara, K. Tsunekawa, D. D. Djayaprawira, N. Watanabe and Y. Suzuki, *J. Appl. Phys.*, **44**, L1237 (2005).
- [27] A. A. Tulapurkar, Y. Suzuki, A. Fukushima, H. Kubota, H. Maehara, K. Tsunekawa, D. D. Djayaprawira, N. Watanabe and S. Yuasa, *Nature*, **438**, 339 (2005).
- [28] H. Kubota, A. Fukushima, K. Yakushiji, T. Nagahama, S. Yuasa, K. Ando, H. Maehara, Y. Nagamine, K. Tsunekawa, D. D. Djayaprawira, N. Watanabe and Y. Suzuki, *Nature Phys.*, **4**, 37 (2008).
- [29] J. C. Sankey, Y.-T. Cui, J. Z. Sun, J. C. Slonczewski, R. A. Buhrman and D. C. Ralph, *Nature Phys.*, **4**, 67 (2008).
- [30] T. Maruyama, Y. Shiota, T. Nozaki, K. Ohta, N. Toda, M. Mizuguchi, A. A. Tulapurkar, T. Shinjo, M. Shiraishi, S. Mizukami, Y. Ando and Y. Suzuki, *Nature Nanotech.*, **4**, 158 (2009)
- [31] Y. Shiota, T. Nozaki, F. Bonell, S. Murakami, T. Shinjo and Y. Suzuki, *Nature Mat.*, **11**, 39 (2012)
- [32] T. Nozaki, Y. Shiota, S. Miwa, S. Murakami, F. Bonell, S. Ishibashi, H. Kubota, K. Yakushiji, T. Saruya, A. Fukushima, S. Yuasa, T. Shinjo and Y. Suzuki, *Nature Phys.*, **8**, 492 (2012).
- [33] S. Kanai, M. Yamanouchi, S. Ikeda, Y. Nakatani, F. Matsukura, H. Ohno, *Appl. Phys. Lett.*, **101**, 122403 (2012).
- [34] Prepared based on G. Bertero, DISCON2011 (HDD) and ITRS (<http://www.itrs.net/>)
- [35] T. Kishi, H. Yoda, T. Kai, T. Nagase, E. Kitagawa, M. Yoshikawa, K. Nishiyama, T. Daibou, M. Nagamine, M. Amano, S. Takahashi, M. Nakayama, N. Shimomura, H. Aikawa, S. Ikegawa, S. Yuasa, K. Yakushiji, H. Kubota, A. Fukushima, M. Oogane, T. Miyazaki and K. Ando, *Tech. Dig. - Int. Electron Devices Meet.* 309 (2008).
- [36] S. I. Kiselev, J. C. Sankey, I. N. Krivorotov, N. C. Emley, R. J. Schoelkopf, R. A. Buhrman and D. C. Ralph, *Nature*, **425**, 380 (2003).

- [37] T. Wada, T. Yamane, T. Seki, T. Nozaki, Y. Suzuki, H. Kubota, A. Fukushima, S. Yuasa, H. Maehara, Y. Nagamine, K. Tsunekawa, D. D. Djayaprawira and N. Watanabe, *Phys. Rev. B*, **81**, 104410 (2010).
- [38] D. Houssameddine, U. Ebels, B. Delaet, B. Rodmacq, I. Firastrau, F. Ponthenier, M. Brunet, C. Thirion, J. P. Michel, L. Prejbeanu-Buda, M. C. Cyrille, O. Reden and B. Dieny, *Nature Mat.*, **6**, 447 (2007).
- [39] F. B. Mancoff, N. D. Rizzo, B. N. Engel, and S. Tehrani, *Nature*, **437**, 393 (2005).
- [40] W. H. Rippard, M. R. Pufall, S. Kaka, T. J. Silva and S. E. Russek, *Phys. Rev. B*, **70**, 100406 (R) (2004).
- [41] W. H. Rippard, M. R. Pufall and S. E. Russek, *Phys. Rev. B*, **74**, 224409 (2006).
- [42] A. M. Deac, A. Fukushima, H. Kubota, H. Maehara, Y. Suzuki, S. Yuasa, Y. Nagamine, K. Tsunekawa, D. D. Djayaprawira and N. Watanabe, *Nature Phys.*, **4**, 803 (2008).
- [43] M. Johnson, *Phys. Rev. Lett.*, **70**, 2142 (1993).
- [44] D. J. Monsma, J. C. Lodder, Th. J. A. Popma, and B. Dieny, *Phys. Rev. Lett.*, **74**, 5260 (1995).
- [45] S. Datta, B. Das, *Appl. Phys. Lett.*, **56**, 665 (1990).
- [46] J. Fabian, I. Zutic, and S. Das Sarma, *Appl. Phys. Lett.*, **84**, 85 (2004).
- [47] S. Sugahara and M. Tanaka, *Appl. Phys. Lett.*, **84**, 2307 (2004).
- [48] H. Bruckel, G. Reiss, H. Binzelberg, M. Bertram, I. Monch and J. Schumann, *Phys. Rev. B*, **58**, R8893 (1998).
- [49] G. E. W. Bauer, A. Brataas and B. J. van. Wees, *Appl. Phys. Lett.* **82**, 3928 (2003).
- [50] S. Matsunaga, J. Hayakawa, S. Ikeda, K. Miura, H. Hasegawa, T. Endoh, H. Ohno and T. Hanyu, *Appl. Phys. Ex.* **1**, 091301 (2008).
- [51] W. Zhao, E. Belhaire, V. Javerliac, C. Chappert, and B. Dieny, *Proc. IEEE Int. Conf. Integr. Circuit Design Technol.*, (2006).
- [52] S. Paul, S. Mukhopadhyay and S. Bhunia, *IEEE/ACM International Conference on Computer-Aided Design*, 589 (2008).
- [53] G. Prenat, W. Guo, M. E. Baraji, V. Javerliac and J. P. Nozières, *IEEE Trans. Magn.* **45**, 3400 (2009).
- [54] L. Leem and J. S. Harris, *J. Appl. Phys.* **105**, 07D102 (2009).
- [55] P. M. Braganca, J. A. Katine, N. C. Enley, D. Mauri, J. R. Childress, P. M. Rice,

- E. Delenia, D. C. Ralph and A. Buhrman, *IEEE Trans. Nanotech.* **8**, (2009).
- [56] J. Z. Sun, M. C. Gaidis, E. J. O'Sullivan, E. A. Joseph, G. Hu, D. W. Abraham, J. J. Nowak, P. L. Trouilloud, Yu Lu, S. L. Brown, D. C. Worledge and W. J. Gallagher, *Appl. Phys. Lett.*, **95**, 083508 (2009).
- [57] Y. Suzuki and H. Kubota, *J. Phys. Soc. Jpn.* **77**, 031002 (2008).
- [58] D. C. Worledge and P. L. Trouilloud, *Appl. Phys. Lett.*, **83**, 84 (2003).
- [59] M. Sato and K. Kobayashi, *J. Appl. Phys.*, **36**, L200 (1997)
- [60] Yu. Lu, R. A. Altman, A. Marley, S. A. Rishton, P. L. Trouilloud, G. Xiao, W. J. Gallagher and S. S. P. Parkin, *Appl. Phys. Lett.*, **70**, 2610 (1997).
- [61] W. J. Gallagher, S. S. P. Parkin, Yu. Lu, X. Y. Bian, A. Marley, K. P. Roche, R. A. Altman, S. A. Rishton, C. Jahnes, T. M. Shaw and G. Xiao, *J. Appl. Phys.* **81**, 3741 (1997).
- [62] J. A. Osborn, *Phys. Rev.*, **67**, 351, (1945).
- [63] J. C. Slonczewski, U. S. patent 5, 695, 864 (9 Dec. 1997).
- [64] H. Tomita, H. Maehara, T. Nozaki and Y. Suzuki, *J. Magnetism* **16**, 140 (2011).
- [65] S. Kasai, K. Nakano, K. Kondou, N. Ohshima, K. Kobayashi and T. Ono, *Appl. Phys. Ex.* **1**, 091302 (2008).
- [66] T. Nozaki, H. Kubota, S. Yuasa, M. Shiraishi, T. Shinjo and Y. Suzuki, *Appl. Phys. Lett.* **95**, 022513 (2009).
- [67] L. Xue, C. Wang, Y. -T. Cui, J. A. Katine, R. A. Buhrman, D. C. Ralph, *Appl. Phys. Lett.* **99**, 022505 (2011).
- [68] S. Petit, C. Baraduc, C. Thirion, U. Ebels, Y. Liu, M. Li, P. Wang and B. Dieny, *Phys. Rev. Lett.* **98**, 077203 (2007).
- [69] E. B. Myers, F. J. Albert, J. C. Sankey, E. Bonet, R. A. Buhrman and D. C. Ralph, *Phys. Rev. Lett.*, **89**, 196801 (2002).
- [70] R. H. Koch, J. A. Katine and J. Z. Sun. *Phys. Rev. Lett.*, **92**, 088302 (2004).
- [71] S. Ishibashi, T. Seki, T. Nozaki, H. Kubota, S. Yakata, A. Fukushima, S. Yuasa, H. Maehara, K. Tsunekawa, D. D. Djayaprawira and Y. Suzuki, *App. Phys. Exp.*, **3**, 073001 (2010).
- [72] S. Yakata, H. Kubota, Y. Suzuki, K. Yakushiji, S. Yuasa and K. Ando, *J. Appl. Phys.* **105**, 07D131 (2009).
- [73] H. Kubota, S. Ishibashi, T. Saruya, T. Nozaki, A. Fukushima, K. Yakushiji, K. Ando, Y. Suzuki and S. Yuasa, *J. Appl. Phys.* **111**, 07C723 (2012).
- [74] D. Dixit, K. Konishi, C. V. Tomy, Y. Suzuki and A. A. Tulapurkar, *Appl. Phys. Lett.* **101**, 122410 (2012).
- [75] J. G. Zhu, X. Zhu and Y. Tang, *IEEE Trans. Mag.* **44**, 125, (2008).

- [76] Y. Nozaki, M. Ohta, S. Tateishi, S. Yoshimura and K. Matsukura, *App. Phys. Exp.*, **91**, 082510 (2007).
- [77] T. Yoshioka, T. Nozaki, T. Seki, M Shiraishi, T. Shinjo, Y. Suzuki and Y. Uehara, *Appl. Phys. Ex.*, **3**, 013002 (2010).

List of Publications

Names written with an underline represents the thesis author

(① Authors, ② Title, ③ Journal, ④ Vol., No, pp. -, and Year.)

- (1) ① Hiroyuki Tomita, Katsunori Konishi, Takayuki Nozaki, Hitoshi Kubota, Akio Fukushima, Kay Yakushiji, Shinji Yuasa, Yoshinobu Nakatani, Teruya Shinjo, Masashi Shiraishi, and Yoshishige Suzuki
② Single-Shot Measurements of Spin-Transfer Switching in CoFeB/MgO/CoFeB Magnetic Tunnel Junctions
③ Applied Physics Express
④ 1, 061303 (2008)
- (2) ① Katsunori Konishi, Takayuki Nozaki, Hitoshi Kubota, Akio Fukushima, Shinji Yuasa, Masashi Shiraishi and Yoshishige Suzuki
② Current-Field Driven “Spin Transistor”
③ Applied Physics Express
④ 2, 063004 (2009)
- (3) ① Seung-Seok Ha, Nam-Hee Kim, Chun-Yeol You, Sukmock Lee, Kenta Ohta, Takuto. Maruyama, Katsunori Konishi, Takayuki Nozaki, Yoshishige Suzuki, and William Van Roy
② Brillouin light scattering study of the magnetic anisotropy in bcc-Fe(100) ultrathin films grown on GaAs(100) surfaces with different reconstructions
③ IEEE. TRANSACTIONS on Magnetism
④ 45, 2527 (2009)
- (4) ① Katsunori Konishi, Takayuki Nozaki, Hitoshi Kubota, Akio Fukushima, Shinji Yuasa, Masashi Shiraishi and Yoshishige Suzuki
② Gain and Fan-out in a Current-Field Driven Spin Transistor With an Assisting AC Magnetic Field
③ IEEE. TRANSACTIONS on Magnetism
④ 48, 1134 (2012)

- (5) ① Dinesh K Dixit, Katsunori Konishi, C. V. Tomy, Yoshishige Suzuki and Ashwin A Tulapurkar
② Spintronic oscillator based on magnetic field feedback
③ Applied Physics Letters
④ **101**, 122410 (2012)
- (6) (minor revision)
① Katsunori Konishi, Dinesh K Dixit, Ashwin A Tulapurkar, Shinji Miwa, Takayuki Nozaki, Hitoshi Kubota, Akio Fukushima, Shinji Yuasa and Yoshishige Suzuki
② RF amplification property of the MgO-based magnetic tunnel junction using field-induced ferromagnetic resonance
③ Applied Physics Letters
- (7) ① 鈴木義茂、小西克典
② ナノスピントロニクス素子の新展開 –トンネル磁気抵抗素子を中心として-
(Progress of Nano-spintronics Devices : Focus on Magnetic Tunnel junctions)
③ 電子情報通信学会誌
④ **95**, 294 (2012)
- (8) ① 小西克典、鈴木義茂
② スピントロニクス評価技術
③ 薄膜の評価技術ハンドブック (テクノシステム、監修：金原繁)
④ p. 294-299 (2013)

List of Conference Presentations

Names written with an underline represents the presenter

(① Authors, ② Title, ③ Conference name, ④ Place, Number and Date)

2012

(1) (poster presentation)

① ◦Katsunori Konishi, Dinesh K Dixit, Ashwin A Tulapurkar, Shinji Miwa, Takayuki Nozaki, Hitoshi Kubota, Akio Fukushima, Shinji Yuasa and Yoshishige Suzuki

② RF amplification properties in magnetic tunnel junctions afforded by field-induced ferromagnetic resonance

③ International Colloquium on Magnetic Films and Surfaces (ICMFS) 2012

④ Fudan Univ. , Shanghai, China, P115, Sep 2012

(2) (poster presentation)

① ◦小西 克典, A. R. Khorsand, 富田 博之, 三輪 真嗣, A. Kirilyuk, A. Kimel, Th. Rasing, 水落 憲和, 鈴木 義茂

② 光学ポンプ・プローブ法を用いた CoFe/Ru/CoFe 反平行結合膜における磁化ダイナミクス測定

③ 第59回春季応用物理学関係連合講演会

④ 早稲田大学、東京、16p-DP4・6、2012年3月

2011

(3) (poster presentation)

① ◦Katsunori Konishi, Dinesh K Dixit, Ashwin A Tulapurkar, Takayuki Nozaki, Hitoshi Kubota, Akio Fukushima, Shinji Yuasa and Yoshishige Suzuki

② RF amplification property in a current-field driven spin transistor

③ 56th annual conference on magnetism and magnetic materials

④ Scottsdale, Arizona, FP-03, Oct 2011

(4) (oral presentation)

① 小西克典, Dinesh K Dixit, Ashwin Tulapurkar, ◦野崎隆行、久保田均、福島章雄、湯浅新治、鈴木義茂

② 磁界誘起FMRによるMTJ素子の高周波電力増幅作用

③ 第35回日本磁気学会

④ 朱鷺メッセ、新潟、29aB-7、2011年9月

(5) (poster presentation)

① ○Katsunori Konishi, Dinesh K Dixit, Ashwin A Tulapurkar, Takayuki Nozaki, Hitoshi Kubota, Akio Fukushima, Shinji Yuasa and Yoshishige Suzuki

② RF amplification in a CoFeB/MgO magnetic tunnel junction by ferromagnetic resonance

③ SPINTECH6

④ Matsue、Shimane FP-44、2011年8月

(5) (poster presentation)

① ○Katsunori Konishi, Dinesh K Dixit, Ashwin A Tulapurkar, Takayuki Nozaki, Hitoshi Kubota, Akio Fukushima, Shinji Yuasa and Yoshishige Suzuki

② RF amplification in a CoFeB/MgO magnetic tunnel junction by ferromagnetic resonance

③ SPINTECH6

④ Matsue、Shimane FP-44、2011年8月

(6) (poster presentation)

① ○小西克典、野崎隆行、久保田均、福島章雄、湯浅新治、鈴木義茂

② 電流磁場駆動型スピントランジスタ

③ スピン流の創出と制御 特定研究会

④ 東京大学、東京、51、2011年1月

2010

(7) (poster presentation)

① ○Katsunori Konishi, Takayuki Nozaki, Hitoshi Kubota, Akio Fukushima, Shinji Yuasa, Masashi Shiraishi and Yoshishige Suzuki

② Fan-out Value in a Current-Field Driven Spin Transistor with an Assisting AC Magnetic Field

③ International Conference of Asian Union of Magnetism Societies (ICAUMS) 2010

④ Jeju, Korea, CP04, Dec 2010

(8) (poster presentation)

① ○Katsunori Konishi, Takayuki Nozaki, Hitoshi Kubota, Akio Fukushima, Shinji Yuasa, Masashi Shiraishi and Yoshishige Suzuki

② Fan-out Value in a Current-Field Driven Spin Transistor with an Assisting AC Magnetic Field

③ International Conference of Asian Union of Magnetism Societies (ICAUMS) 2010

④ Jeju, Korea, CP04, Dec 2010

(9) (poster presentation)

① ○Katsunori Konishi, Takayuki Nozaki, Hitoshi Kubota, Akio Fukushima, Shinji Yuasa, Masashi Shiraishi and Yoshishige Suzuki

② Fan-out Value in a Current-Field Driven Spin Transistor

③ Solid State Devices and Materials (SSDM) 2010

④ Tokyo Univ. Tokyo, Japan, P-12-2, Sep 2010

(10) (oral presentation)

① ○小西克典、野崎隆行、久保田均、福島章雄、湯浅新治、白石誠司、鈴木義茂

② 電流磁場駆動型スピントランジスタ II・交流磁場下におけるファンアウト値の検証・

③ 第 7 1 回秋季応用物理学関係連合講演会

④ 長崎大学、長崎、16a-A-6、2010 年 9 月

(11) (oral presentation)

① ○小西克典、野崎隆行、久保田均、福島章雄、湯浅新治、白石誠司、鈴木義茂

② 電流磁場駆動型スピントランジスタにおけるファンアウト値

③ 第 3 4 回日本磁気学会

④ つくば、茨城、7pB-10、2010 年 9 月

2009

(12) (oral presentation)

① ○小西克典、野崎隆行、久保田均、福島章雄、湯浅新治、白石誠司、鈴木義茂

② 電流磁場駆動型スピントランジスタ

③ 第 33 回日本磁気学会

④ 長崎大学、長崎、13pA-5、2009 年 9 月

(13) (poster presentation)

① ○Katsunori Konishi, Takayuki Nozaki, Hitoshi Kubota, Akio Fukushima, Shinji Yuasa, Masashi Shiraishi and Yoshishige Suzuki

② Fan-out Value in a Current-Field Driven Spin Transistor with an Assisting AC Magnetic Field

③ International Colloquium on Magnetic Films and Surfaces (ICMFS) 2009

④ Freie University, Berlin, Germany, P-We78, Jul 2009

(14) (oral presentation)

- ① ○小西克典、野崎隆行、久保田均、福島章雄、湯浅新治、白石誠司、鈴木義茂
- ② 電流磁場駆動型スピントランジスタ
- ③ 第 56 回春季応用物理学会
- ④ 筑波大学、茨城、1p-TB-2、2009 年 3 月

2008

(15) (oral presentation)

- ① ○小西克典、富田博之、太田健太、丸山拓人、野崎隆行、白石誠司、鈴木義茂
- ② コプレーナウェーブガイドを用いた微小磁性体の FMR 測定
- ③ 第 55 回春季応用物理学会
- ④ 中央大学、千葉、29-p-F-12、2008 年 3 月

List of Grant

(1) Research Fellowships of the Japan Society for the Promotion of Science (JSPS)
for Young Scientists (DC1) with JSPS KAKENHI (Grant No. 22.1632)
Apr. 2010 - Mar. 2013

(2) Institutional Program for Young Researcher Overseas Visits (JSAP),
Development of International Network for Training of Young Researchers
Exploring Multidisciplinary Fields
Sep. 2011 - Oct. 2011

